Atmospheric Transit of a Hypersonic, Axisymmetric, Spin Stabilized Vehicle

by

Peter Kaloupis

A thesis submitted in partial fulfillment
of the requirements for the degree of

Master of Science
in Aeronautics and Astronautics

University of Washington

1989

Approved by Adam Bruckner
(Chairperson of Supervisory Committee)

Program Authorized to
Offer Degree DEPARTMENT OF AERONAUTICS
AND ASTRONAUTICS

Date 12/13/89

In presenting this thesis in partial fulfillment of the requirements for a Master's degree at the University of Washington, I agree that the Library shall make its copies freely available for inspection. I further agree that extensive copying of this thesis is allowable only for scholarly purposes, consistent with "fair use" as prescribed in the U.S. Copyright Law. Any other reproduction for any purpose or by any means shall not be allowed without my written permission.

Signature Peter Kaloupis

Date 14/12/89

University of Washington

Abstract

Atmospheric Transit of a Hypersonic, Axisymmetric, Spin Stabilized Vehicle

by **Peter Kaloupis**

Chairperson of the Supervisory Committee: Research Professor Adam P. Bruckner
Department of Aeronautics andAstronautics

The atmospheric transit of a hypersonic, axisymmetric, spin stabilized vehicle is investigated with special attention to stability considerations. The analysis is valid for general vehicle shapes and Mach number ranges from $10 \leq M_\infty \leq \infty$. The particular case study performed is for the Ram Accelerator Mass Launcher vehicle. It is a chemical mass launcher concept that has been developed at the University of Washington for accelerating vehicles to velocities as high as 10 km/sec for launch to Low Earth Orbit. The force system acting on the vehicle is presented in detail, including Magnus and ablation side forces, and the full six degree of freedom equations of motion are solved numerically to determine the stability characteristics of the Ram Accelerator Mass Launcher vehicle. The Embedded Newtonian theory is used to determine the steady and non-steady aerodynamic characteristics of the vehicle for various configurations. An analysis of the heat transfer to the vehicle is performed for radiative and convective heating, with special attention to the effects of ablation on vehicle stability. It is shown that the current configuration of the Ram Accelerator Mass Launcher vehicle is dynamically unstable and cannot be spin stabilized. Recommendations are made for a more stable vehicle design.

TABLE OF CONTENTS

LIST OF FIGURES

LIST OF SYMBOLS

B	blowing parameter, Equation 5.1.4
C_A	axial force coefficient, $C_A = 8\ A / \rho_\infty U_\infty^2\ \pi d^2$
C_D	drag coefficient, $C_D = C_A \cos\alpha + C_N \sin\alpha$
C_{D_n}	nose drag coefficient, Equation 4.1.1.15
C_γ	empirical Newtonian pressure coefficient, Equation 4.1.1.5
C_m	pitching moment, $C_m = 8\ M / \rho_\infty U_\infty^2\ \pi d^3$
C_{m_θ}	total damping derivative
C_N	normal force coefficient, $C_N = 8\ N / \rho_\infty U_\infty^2\ \pi d^2$
C_{N_p}	Magnus moment coefficient, $C_{N_p} = 8\ N_p / \rho_\infty U_\infty^2\ \pi d^3\ (pd/2V)$
C_p	pressure coefficient, $C_p = (p - p_\infty) / \rho_\infty U_\infty^2 /2$
C_{p_o}	blast wave pressure coefficient, Equation 4.1.1.3
C_q	dynamic damping derivative
C_{Y_p}	Magnus force coefficient, Equation 4.2.1.6
d	body diameter
f^*	dynamic pressure ratio, Equation 4.1.1.8
g	gravity
g^*	hypersonic velocity ratio, Equation 4.1.1.9
H	total enthalpy
h	Magnus term, Equation 4.2.1.3
	static enthalpy
I	moment of inertia
K^*	hypersonic constant, Equation 4.1.1.14
L	body length
	x moment
l_v	Rosseland mean free path
M	Mach number
	y Moment
m	mass flow rate
	vehicle mass
N	yaw moment
p	pressure

	roll rate
q	pitch rate
	heat flux, Equations 5.1.1and 5.2.1
R	radius, Equation 4.1.1.12
r	body radius
	yaw rate
Re	Reynolds number, $Re = \rho U x / \mu$
Rsh	shock radius, Equation 4.1.1.11
S_d	dynamic stability factor, Equation 6.2.1
S_g	gyroscopic stability factor, Equation 6.1.1
T	temperature
U	velocity
u	x body axes velocity
	tangential surface velocity
V	velocity, $V^2 = u^2 + v^2 + w^2$
v	y body axes velocity
	normal surface velocity
w	z body axes velocity
X	x body axes aerodynamic forces, Equation A.3
x	body position
Y	y body axes aerodynamic forces, Equation A.3
Z	z body axes aerodynamic forces, Equation A.3

Greek

α	angle of attack, Equation 2.1.1
β	yaw angle, Equation 2.1.2
γ	ratio of specific heats
Δ	shock detachment distance
δ	boundary layer thickness, Equation 4.2.1.5
θ	Euler angle about y axis
λ	latitude
μ	longitude
ρ	density

σ	Stefan-Boltzmann constant
τ	dimensionless optical length
ϕ	Euler angle about x axis
	circumferential angle
φ	ablative heat reduction parameter, Equation 5.1.6
χ^*	hypersonic similarity parameter, Equation 4.1.1.7
ψ	Euler angle about z axis
	Rosseland mean free path, Equation 5.2.2
ω	angular velocity

Subscripts

∞	free stream conditions
n	nose
α	derivative with respect to angle of attack
E	body element in embedded flow field
r	reference value
b	maximum body diameter
E	Earth fixed axes
B	body fixed axes
CG	center of gravity
V	vehicle axes
x	x body axis
y	y body axis
z	z body axis
a	after body
w	wall region
s	stagnation region

ACKNOWLEDGEMENTS

The author wishes to express his sincere appreciation to his advisor Professor Adam P. Bruckner and Professor Abraham Hertzberg for their guidance, support, and encouragements during this investigation. Special thanks are due to my fellow Research Assistants who have patiently performed my duties and undertaken my responsibilities during the completion of this thesis. They are Alan E. Kull, Edward A. Burnham Jr., Gilbert Chew, Erik C. Christofferson, Barbrina L. Dunmire and Jacqueline Auzias de Turenne, Amy E. Prochko, H. Andrew Berschauer, and Robert Macintosh. Thanks also to Moeljo Soetrisno for motivational support, to Brian Lewis for doubting that it could be done, and to Paul Cacciola who endured the hardships of life without computing during the completion of this report.

DEDICATION

Mom and Dad.

Chapter 1

Introduction

1.1 Background

The problem of determining the motion of a projectile through the atmosphere has been studied by ballisticians for several centuries, but has only recently received the attention of aerodynamicists. Early studies of projectile motion had failed to realize the magnitude of the aerodynamic forces, in particular the drag, and included only the effects of the force of gravity. Thus, determinations of projectile range and velocity gave large and systematic errors. After the importance of air resistance was recognized, the fundamental paper of Fowler, Gallop, Lock, and Richmond [1] became the basis of modern exterior ballistics.

Since then, however, the size of the projectiles and the velocities that they could achieve have been increasing steadily. Projectiles gave way to larger vehicles, whose aerodynamic characteristics included lift and thrust forces, and in the case of spinning vehicles Magnus forces as well. These new vehicles required new techniques for determining the forces, and more thorough investigations were performed - most notably by McShane, Kelley, and Reno [2], and Davis, Follin, and Blitzer [3], who give an excellent treatise on the subject. However, as the Mach number increased, the techniques of these authors failed to accurately predict the aerodynamic coefficients. The velocities of the vehicles studied by these authors, typically less than 1500 m/sec, are still moderate by today's standards. As the upper velocity limit increased into the high supersonic and hypersonic regimes, the problem of determining the aerodynamic characteristics for the vehicle motion became more and more complicated. With hypersonic vehicle technology increasing in importance in a variety of applications, such as future space transportation systems, hypersonic transports, and re-entry vehicles, the problems associated with hypersonic flight gained more attention.

The characteristic problems of hypersonic flow are the hydrodynamic effects due to the high Mach number, and physical effects due to the large energies associated with the flow. Hydrodynamic problems include the nature of the flow field in the inviscid region, which can no longer be considered isentropic and irrotational because of the large entropy gradients through the strong bow shock. In addition, the inviscid flow region is greatly reduced because of the thicker boundary layers and the nearness of the shock to the body. Physical problems are associated with the high temperatures generated by the strong shocks. In this regime air no longer behaves as an ideal gas, and the effects of heat transfer to the vehicle cannot be neglected.

At hypersonic Mach numbers the effects of viscous aero stresses give rise to finite thickness shock layers which further complicate the analysis, and the effects of mass addition into the boundary layer due to ablation of the surface can significantly alter the aerodynamic characteristics of such vehicles. Effects such as Magnus forces and ablation side forces in turbulent flow need to be considered, and it is these special considerations at the hypersonic Mach numbers, and how they affect vehicle motion, that are being considered here.

1.2 Present Work

Many types of external vehicle configurations exist for atmospheric transit. These include finned vehicles that employ aerodynamic surfaces for stability and control, as well as axisymmetric configurations that rely on spinning for stability. They may be lifting bodies, and may include thrust forces. This thesis will restrict itself to the case of an axisymmetric, hypersonic, spin stabilized vehicle flying at some angle of attack, with no thrust force, operating in the Mach number range $10 \leq M_\infty \leq 30$. The treatment is analytical and semi-empirical in nature, and does not require the extensive computing time associated with computational fluid dynamic techniques. The method presented here is well suited for the present stage of the analysis. Methods of solution for finding aerodynamic coefficients will be presented with justification, and the six degree of freedom equations of motion will be given with a discussion of the forces and moments acting on the vehicle with varying Mach number and angle of attack. Although the analysis is general and is amenable to any hypersonic axisymmetric vehicle, the particular case study performed is for the Ram Accelerator Mass Launcher vehicle.

The Ram Accelerator is a chemically propelled mass driver which is being presented as a viable new approach for directly launching acceleration insensitive materials into low Earth orbit [4-6]. It is a ramjet-in-tube concept developed at the University of Washington that provides a unique method for accelerating vehicles to velocities as high as 10,000 m/sec [7-12]. The external configuration of such a vehicle is predetermined by the necessary requirements for the propulsive cycles it must undergo, and it consists of a conical forebody, a cylindrical midsection, and a truncated cone boatail, as shown in Fig. 1. This thesis, however, will restrict itself to the case of a conical nose with a cylindrical afterbody and no boatail, also shown in Fig. 1, since the present technique of determining aerodynamic coefficients cannot account for negative body angles. The effects of boatailing on stability will be discussed qualitatively in Chapter 7.

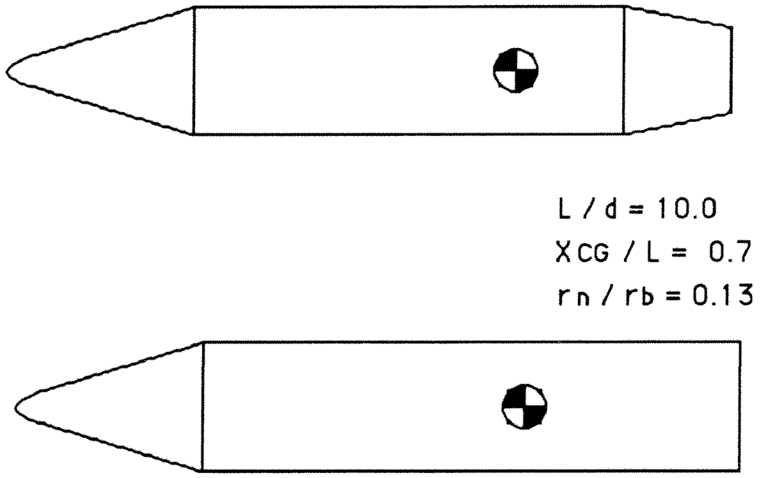

Figure 1. Vehicle Configuration

Chapter 2 discusses the pertinent reference frames for the analysis, and gives the required equations of motion. The force system and moments acting on the body are presented in Chapter 3, with a qualitative discussion of the forces. Chapter 4 presents the methods selected for determining the required aerodynamic coefficients for solving the equations of motion, and discusses their justification. Chapter 5 details the effects of aerodynamic heating to the vehicle, both radiative and convective, as well as the effects of ablation on vehicle motion and stability. The stability conditions and constraints for spinning vehicles are presented in Chapter 6, and the results of the analysis are presented in Chapter 7 with a discussion of the effects of configuration changes. Conclusions and recommendations are made in Chapter 8.

Chapter 2

Reference Frames and the Equations of Motion

When solving for the atmospheric transit of a vehicle, a number of reference frames are important for specifying relative positions and velocities. The reference frames used in this analysis are defined below, with an explicit definition of the Earth fixed inertial frame required for determining the equations of motion. The derivation of the six degree of freedom equations of motion is performed by Etkin [13], and the results are presented here.

2.1 Reference Frames

In many problems of atmospheric transit the rotation of the Earth and its curvature may be entirely neglected. However, in the case of hypervelocity problems, although we can neglect the Earth's rotation in the moment equations, it must be included in the force equations for accurately determining vehicle motion. The justification for this is given in Chapter 3, where the force system is presented in detail. Here it is sufficient to simply state this in order to select an inertial frame of reference.

The natural choice of inertial frames for problems where the rotation of the Earth is deemed important is shown in Fig. 2. It is denoted F_E and it is a coordinate system whose origin lies at the mass center of the Earth, and whose axes are fixed by a reference point on the equator and the Earth's axis. At this point it is convenient to introduce the vehicle carried vertical frame F_V also shown in Fig. 2. It is attached to the vehicle center of mass, and is oriented such that the z axis points vertically downward in the radial direction and coincides with the g vector. The relative position of the vehicle frame to the Earth frame can be given by two angles, λ and μ, which are the latitude and longitude of the point where the z axis of the vehicle frame intersects the Earth's surface. The axis of the Earth is fixed in inertial space, and the Earth rotates about it with some angular velocity ω^E.

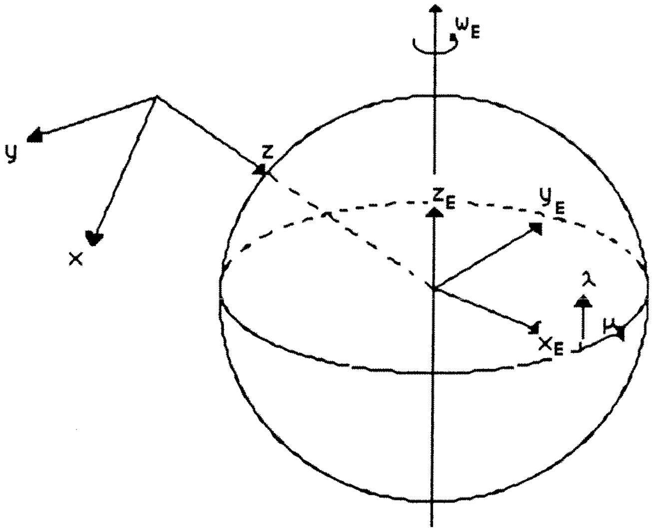

Figure 2. Earth Fixed and Vehicle Fixed Reference Frames

The body axes frame F_B has its origin at the vehicle mass center, and is aligned with the vehicle plane of symmetry and the principal axes, with the z axis pointing downward. The body axes system is shown in Fig. 3 and has the notation shown associated with it. The body axes rotate with the vehicle with an angular velocity of (p,q,r) and translate with respect to the inertial frame with the velocity (u,v,w). The orientation of the body axes frame relative to the vehicle vertical frame can be given by three consecutive rotations about the axes z,y, and x as shown in Fig. 4. They are a rotation ψ about the z axis, a rotation θ about the y axis, and a rotation ϕ about the x axis. These are the Euler angles that bring the two frames into coincidence, and are important for determining the components of the aerodynamic forces.

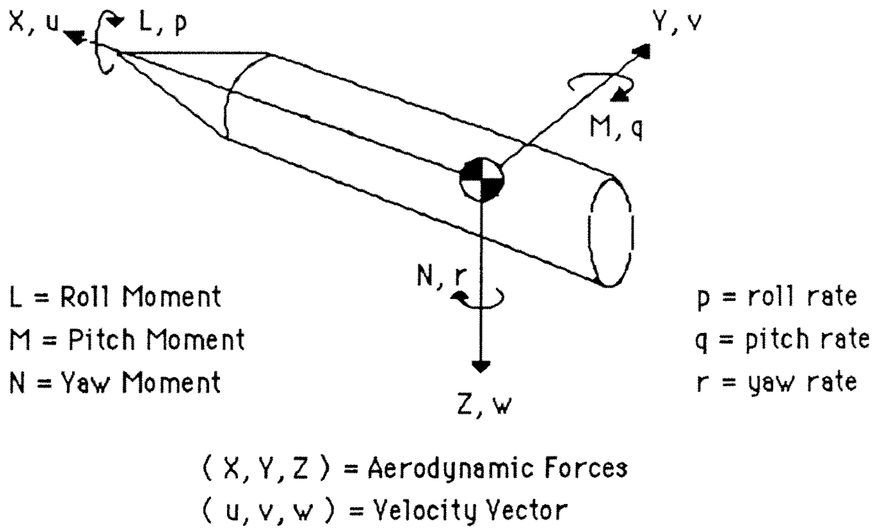

Figure 3. Body Fixed Reference Frame with Associated Notation

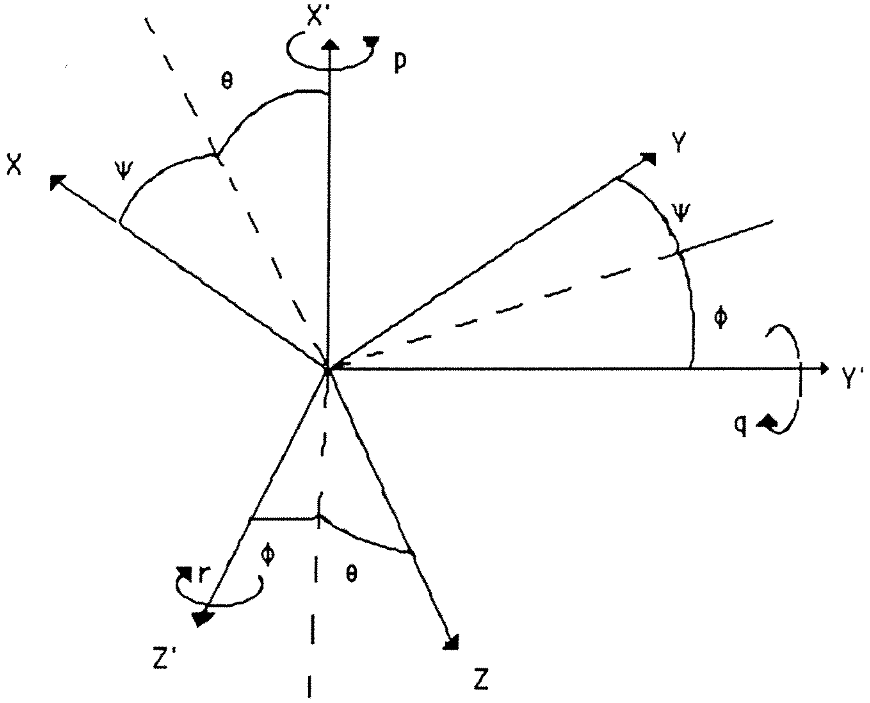

Figure 4. Vehicle Euler Angles for Body Axes Co-ordinate System

Given the body axes frame we can also define two aerodynamic angles, the angle of attack and the sideslip angle, which are defined in this coordinate system as:

$$\alpha = \tan^{-1} \frac{w}{u} \tag{2.1.1}$$

$$\beta = \sin^{-1} \frac{v}{V} \tag{2.1.2}$$

Then the velocity components with respect to these angles can be written:

$$u = V \cos \beta \cos \alpha \tag{2.1.3}$$

$$v = V \sin \beta \tag{2.1.4}$$

$$w = V \cos \beta \sin \alpha \tag{2.1.5}$$

Any vector within a particular reference frame may be given in any other frame by undergoing a rotation under a transformation matrix, and thus with the reference frames defined we can proceed to write the equations of motion.

2.2 Equations of Motion

The equations of motion provide the mathamatical model which describes the general motion of the vehicle. With knowledge of the rate of change of momentum, rate of change of angular momentum, and the aerodynamic forces, we can write down the equations of motion. There are two sets of fundamental equations, the force equations and the moment equations. The force equations can be found from the requirement that the sum of external forces in a given direction is equal to the time rate of change of translational momentum in that direction, and the momentum equations are found from the requirement that the sum of external moments in a given direction is equal to the time rate of change of the angular momentum in that direction.We can write for the force equations:

$$X - m\,g \sin\theta = m\,[\,\dot{u} + (q_B^E + q)\,w - (r_B^E + r)\,v\,] \tag{2.2.1}$$

$$Y + m\,g \cos\theta \sin\phi = m\,[\,\dot{v} + (r_B^E + r)\,u - (p_B^E + p)\,w\,] \tag{2.2.2}$$

$$Z + m\,g \cos\theta \cos\phi = m\,[\,\dot{w} + (p_B^E + p)\,v - (q_B^E + q)\,u\,] \tag{2.2.3}$$

where the terms with the superscript E denote quantities associated with the rotation of the Earth. The moment equations may be written for a rigid body with principal axes and axisymmetric symmetry as:

$$L = I_x \dot{p} \tag{2.2.4}$$

$$M = I_y \dot{q} - (I_z - I_x)\, r\, p \tag{2.2.5}$$

$$N = I_z \dot{r} - (I_x - I_y)\, p\, q \tag{2.2.6}$$

where I_x, I_y, and I_z are the principal moments of inertia.

So far we have said nothing about the aerodynamic forces X,Y, and Z that appear in the above equations. The forces on the vehicle depend on the local density of the air and the local motion of the vehicle relative to the atmosphere, hence on u,v, and w. These forces will be discussed in detail in the following chapter, and their components in the x, y, and z directions can then be substituted in for X, Y, and Z by applying the transformation matrix. A similar analysis can be done for the moment equations. The complete list of simultaneous equations that need to be solved for the vehicle motion are presented in Appendix A.

Chapter 3

Force System

As the vehicle transits the atmosphere it will experience forces and moments acting upon it. All we need to know to characterize these forces and moments is the mass distribution of the vehicle. Its center of mass, its radius of gyration about the center of mass, and the relevant forces that are acting on the vehicle must be known. These forces can be divided into two distinct classes, those due to gravitational and non-inertial reference frame accelerations and those due to aerodynamic forces, caused by the movement of air about the vehicle.

3.1 Gravitational and Coriolis Forces

It is obvious that, when writing the force vector for atmospheric flight, the weight mg must be considered as a contributing factor. It is somewhat less obvious what contribution the centripetal acceleration, the rotation of the Earth, and the Earth's curvature make to the force vector. A number of equations that describe the acceleration of the vehicle center of mass with respect to the inertial frame can be presented. The accelerations include:

1) the acceleration of the mass center relative to the moving frame,
2) the acceleration of the mass center due to the rotation of the moving frame,
3) the centripetal acceleration of the mass center relative to the moving frame,
4) the acceleration of the origin of the moving frame,
5) and the Coriolis acceleration of the moving frame.

If we examine these terms more carefully we can see the relative magnitude of these as compared to the weight mg.

If we consider the vehicle fixed reference frame we can see that the first three terms will be zero, since the frame is fixed to the vehicle center of mass, and there are no accelerations of the mass center with respect to the vehicle fixed reference frame. The two terms left are the acceleration of the vehicle fixed frame itself and the Coriolis acceleration. The first of these is just the centripetal acceleration associated with the Earth's rotation. This term varies in magnitude from zero at the poles to 1/1000 mg at the equator, and can therefore be neglected. For the Coriolis acceleration we need to look at the z component of the equations of motion. If we consider Equation 2.2.3 with the Euler angles zero for horizontal flight at the equator then:

$$- Z + mg = m\, V\, (q^E_B + q) \qquad 3.1.1$$

since v = w = 0 and V = u. Then from Equations A.2 and A.8 $q^E{}_B = - \omega^E$ and P = Q = R = 0. From Equation A.7 we know that $q = - (\omega^E + \mu)$, and A.6 gives $\mu = V / R$. Hence for the force equation in the z direction we have:

$$- Z + mg = 2\, m\, V\, \omega^E + \frac{m\, V^2}{R} \qquad 3.1.2$$

The first term on the right hand side is the Coriolis force due to the Earth's rotation. At orbital speed, approximately 7.9 km/sec, it is equal to 1/10 mg. The second term is due to the curvature of the Earth, and at orbital speed is equal to 9/10 mg. It is clear that if the gravitational force is to be included in the analysis, then the Coriolis force must also be included. For low velocities these terms become negligible, and indeed at speeds that corespond to Mach numbers $M_\infty \leq 3$ at sea level each term amounts to only 1/100 mg and may be neglected. This argument is relevant only for the force equations, and has validity only for flight path calculations. If we are interested solely in attitude dynamics, these terms in the moment equations become negligible, since the rotation rate of the Earth is entirely negligible when compared to any practical vehicle rotation.

3.2 Aerodynamic Forces and Moments

The aerodynamic forces arise due to the movement of air over the vehicle. They can be broken down into pressure forces and viscous forces, and when the vehicle center of pressure does not coincide with the vehicle center of mass they can give rise to moments. The forces and moments are discussed in this chapter qualitatively, and their magnitude will be considered in the following chapter, where the aerodynamic coefficients will be found in order to solve the equations of motion. The methods selected for determining the coefficients are presented in this chapter, with a justification for their use. The aerodynamic forces and moments that are important in determining vehicle motion are:

1) the lift and drag forces and moments,
2) the pitch and yaw moments and damping moments,
3) the Magnus side force and moment,
4) and the ablation side force.

When dealing with an axisymmetric body it is generally more sensible to speak in terms of normal and axial forces as opposed to lift and drag forces, since they are aligned with the natural co-ordinate system of the vehicle. They are related through:

$$D = A \cos \alpha + N \sin \alpha \qquad 3.2.1$$

$$L = N \cos \alpha - A \sin \alpha \qquad 3.2.2$$

3.2.1 Pressure Forces and Moments

3.2.1.1 Forces

The lift and drag forces are the most important forces that act on the vehicle. We can determine the magnitude of these forces if we know the pressure distribution C_p over the vehicle, since we can then integrate the pressure distribution to find the forces. Determining the forces due to pressure is then tantamount to finding an accurate representation of the pressure distribution.

Various methods exist for finding the pressure distribution about axisymmetric vehicles. These include the small perturbation method [14], and the first and second order theories of Van Dyke [15], among others. However, these are restricted to supersonic Mach numbers and at hypersonic velocities different techniques must be used for finding the pressure distribution over an axisymmetric vehicle. The most fundamental of these is the Newtonian impact theory [16], which assumes that the fluid particles do not interact with each other and that the only change in velocity of a particle impinging on the body is in the normal direction to the surface. The normal component of momentum is transferred to the body, and the particle moves along the surface of the body with no tangential acceleration. For blunted bodies, or bodies with curved surfaces, it was noted by Busemann [17] that a centrifugal pressure correction term must be added to account for accelerations due to the curved particle paths. A central assumption in these theories is that the Mach number approaches ∞, and that γ approaches unity. Further, these theories assume that the shock layer is thin and that the shock lies close to, or on the body. For hypersonic axisymmetric or blunted bodies this is not always the case, and a different technique must be used for determining the pressure distribution over the vehicle.

To remove these limitations Seiff proposed the Embedded Newtonian technique [18]. In this theory, developed for steady flow, a nonuniform rotational inviscid flow field is defined downstream of the bow shock, whose shape is determined by the nose shape and drag coefficient. The pressure on the body is then determined by generalized Newtonian theory. This method takes into account the reduction in dynamic pressure and velocity that arise due to the entropy layer caused by the bow shock. Ericsson extended this method to include unsteady effects and large nose bluntness at finite Mach numbers [19-22]. The Busemann correction to the embedded flow field has been considered by Tong and Hui [23], but it has been shown that the pressure correction term is overestimated and the conditions that Mach number is ∞ and γ is unity are not satisfied over most of the vehicle. In addition, Tong and Hui have employed relationships for velocity and density ratios across the shock that correspond to the strict Newtonian limit, and cannot therefore account for finite Mach number dependence.

The flowfield over the vehicle, except in the immediate vicinity of the stagnation point, is approximated by a strong curved bow shock whose shape is determined by nose geometry, together with an inviscid shear flow downstream of the shock where pressures are determined using simple Newtonian concepts. Thus, following the recommendation of East and Hutt [24], the method selected for determining the pressure distribution for current conditions is that of Ericsson [22]. This method provides excellent agreement between theory and experiment for pressure distributions and stability coefficients at the high Mach numbers of interest for blunt bodies.

3.2.1.2 Aerodynamic Moments

The lift and drag forces due to the pressure distribution over the vehicle act through the center of pressure, and when this does not coincide with the center of gravity, moments are created about the vehicle mass center. These moments are important in determining the vehicle stability, and are found by integrating the pressure distribution with respect to some moment arm over the vehicle surface. The non-steady Embedded Newtonian method of Ericsson provides for finding these stability coefficients over a broad range of vehicle shapes, attitude, and flow conditions.

The pitching moment C_m arises because the normal force on the body does not act through the center of gravity. On its own it is one of the most significant contributions to vehicle stability or instability, as will be shown in Chapter 7. In addition, when the vehicle is pitched it has an increased angle of attack over the rear portion of the body, which feels a force that induces a moment about the vehicle center of mass to stop the rotation. This moment is the pitch damping moment C_{m_q} and for long bodies can be quite large. The total damping moment C_{m_θ} is the moment associated with the pitching rate q, plus the moment due to the effects of the time rate of change of angle of attack α. The method of finding these moments about the vehicle center of mass is that given by Ericsson [22] and is presented in Chapter 4.

3.2.2 Viscous Forces and Moments

Viscous forces are created by the shear stresses on fluid particles within the boundary layer. These include Magnus forces and skin friction drag, as well as the effects of mass introduction into the boundary layer, which alters the velocity profiles and pressure gradients about the vehicle and can give rise to side forces.

3.2.2.1 Magnus Force and Moment

Magnus forces and moments are generated by the distorted boundary layer about a spinning body at angle of attack, and are proportional to the spin rate and the angle of attack. The Magnus force is typically small, up to 1/10 of the normal force. It is important because it gives rise to a moment which may be of sufficient magnitude to cause the vehicle to become dynamically unstable. The Magnus force is perpendicular to the lift plane on axisymmetric spinning bodies. It arises purely because of viscous effects and, as postulated by Sedney [25], is caused by the asymmetric boundary layer about the vehicle. This is shown schematically in Fig. 5. The vehicle is at some angle of attack as shown by the cross flow velocity. When there is no spin the boundary layer is symmetric with respect to the plane of angle of attack. When spin is imparted to the vehicle the boundary layer will distort and become assymetric with respect to the plane of angle of attack. This gives rise to asymmetric pressure distributions on the body, and the centrifugal pressure gradient caused by the acceleration of the particles in the radial direction must also be considered. The effects of a circumferential skin friction variation may not be neglected and have to be accounted for in a Magnus theory.

The Magnus moment does not act through the center of pressure since it is a side force. Its moment arm is different from that of the pitching moment, and for a given vehicle configuration and center of gravity position the effects of vehicle variation in length and center of gravity will have opposite effects on stability. For static stability it is desirous to have the center of gravity forward, and for dynamic stability it is desirous to have it aft, as will be shown in Chapter 7.

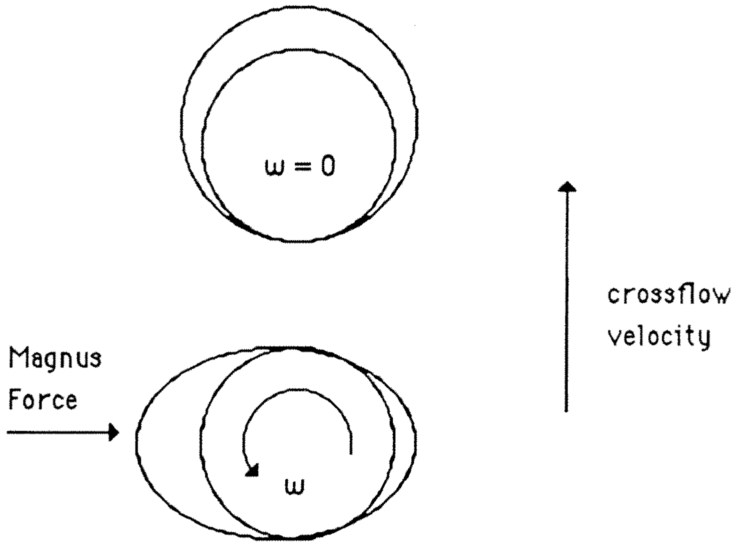

Figure 5. The Magnus Effect on a Spinning Body of Revolution

The Magnus problem is a three-dimensional effect at angle of attack, and therefore the three-dimensional boundary layer must be solved over the vehicle. Most methods of determining the Magnus force and moment have therefore been numerical in nature, and such work was performed by Clark [26], and Dwyer and Sanders [27], using the finite element method. Other investigators have used parabolized Navier-Stokes methods [28-30]. Vaugn and Reiss [31] have developed an approximate analytical method which is especially useful for engineering design purposes. Theirs is the only theory that can account for turbulence effects in a straight forward manner, since turbulence modelling in computational techniques is still a subject of investigation.

The method of Vaugn and Reiss [31] includes the boundary layer displacement thickness distortion and radial pressure gradient effects. They do not consider the effects of shear flow variation on either side of the vehicle, however the overall Magnus force predicted is the same as that of the more complicated analyses. This may be fortuitous since the physical mechanisms for the Magnus forces are asumed to be different. In any case, the theory predicts the magnitude of the Magnus force quite well when compared to experimental results. A similar analysis to that performed by Vaugn and Reiss is performed here, and it is extended and modified for the case of a turbulent boundary layer. It includes a term that takes into account the velocity profile over the cone in order to include the effects of nose blunting. It should be noted that this method tends to underpredict the Magnus effects at very high Mach numbers, however its usefulness cannot be denied.

3.2.2.2 Skin Friction

The effects of skin friction are important for determining drag and heat transfer to the sidewalls of the vehicle, but at high Mach numbers the other contributing factors are of greater importance. In the current hypersonic flow problem the dominant drag forces will be pressure drag and wave drag, and indeed even at Mach numbers of $M_\infty = 10$ these account for almost the entire drag term, and the skin friction contribution may be neglected [32]. The heat transfer to the vehicle has been found based on semi-empirical techniques, and absolute knowledge of the skin friction coefficient is not required.

The skin friction in the stagnation region, however, is of critical importance. It can dictate the ablation and flow characteristics in that region. These effects are discussed with ablation in Chapter 7.

3.2.2.3 Ablation Side Force

The injection of mass by ablation into the boundary layer can influence the aerodynamic characteristics by changing the shearing stresses and the induced pressure due to boundary layer displacement effects. Significant Magnus-like forces can arise due to the combined effects of angle of attack, ablation, and spin [32,33]. Due to thermal lag, the rate of ablation on one side of a spinning body at angle of attack would be higher than on the other side. The difference in ablation rates will create a difference in the boundary layer induced pressure and produce a side force and moment. The side force in this case would act in a direction opposite to that of a classical Magnus force. The magnitude of this side force has been investigated experimentally and is typically at most 1/100 of the normal force [32]. There are no effective techniques of predicting the magnitude of this side force to date, however if the mass flow rate is low it may be neglected.

Chapter 4

Determination of the Aerodynamic Coefficients

The aerodynamic forces and moments are generally characterized by a number of corresponding coefficients that are defined as the ratio of the magnitude of the force to the dynamic pressure, normalized by the vehicle crossectional area. In order to determine these aerodynamic coefficients the flow field about the vehicle must be known, or more precisely the pressure coefficient over the entire vehicle must be known. Computational fluid dynamic techniques are time consuming, and may be limited in regards to the range of conditions over which they may apply. There is, however, suprisingly good agreement between some semi-empirical methods and experimental data. It is this approach that is employed here.

4.1 Pressure Force Coefficients

The methods selected for determining the various aerodynamic coefficients required for the analysis are presented below. A complete derivation of each method is performed in the indicated references and is not repeated here. The force coefficients are found first, followed by the determination of the moment coefficients.

4.1.1 Forces

In order to determine the forces acting on the vehicle the pressure distribution over the entire vehicle must be known. The method selected for finding the pressure force coefficients and subsequently the stability derivatives of the vehicle is the Embedded Newtonian technique developed by Ericsson [22], which is valid for sharp or blunted axisymmetric bodies in the Mach number range $3 \leq M_\infty \leq \infty$.

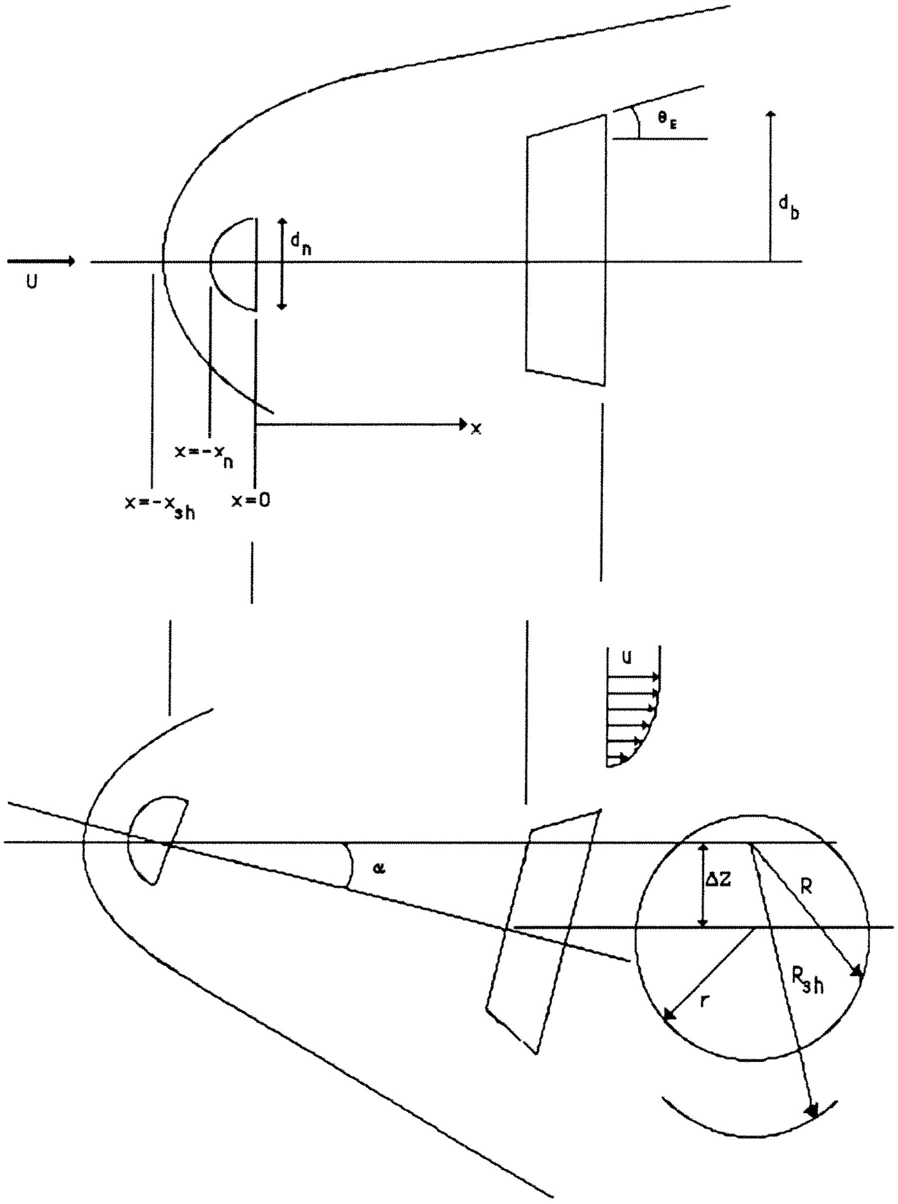

Figure 6. The Embedded Body in a Hypersonic Shock Layer

The coeficient of pressure on the "embedded" body element A shown in Fig. 6 can be written as:

$$C_{p_E} = C_{p_0} + C_\gamma C_{p_{max}} \left(\frac{v}{u}\right)^2 \frac{\rho u^2}{\rho_\infty U_\infty^2} \qquad 4.1.1.1$$

where v is the local velocity component normal to the surface and u is the axial velocity component. For the element A pitching at q rad/sec this is defined geometrically as:

$$\frac{v}{u} = \cos\alpha \sin\theta_E + \sin\alpha \cos\theta_E \sin\phi + \left(\frac{x - x_{CG} + r\tan\theta_E}{u}\right) q \cos\theta_E \sin\phi \qquad 4.1.1.2$$

C_{p_0} is the blast wave pressure coefficient generated downstream of the blunt nose that would exist on an embedded cylinder, and the second term is due to the local body shape embedded in the flowfield. C_{p_0} is given by:

$$C_{p_0} = \frac{0.081\, C_{D_n}^{1/2}}{\frac{x}{d_n} - \frac{x_{sh}}{d_n}} - \frac{0.64}{M_\infty^2} \qquad 4.1.1.3$$

$C_{p_{max}}$ is the modified Newtonian impact pressure and is given by the stagnation pressure behind a normal shock, which for Mach numbers of Newtonian interest $M \geq 3$ can be written:

$$C_{p_{max}} = \frac{\gamma + 3}{\gamma + 1}\left[1 - \frac{1.5}{\gamma + 3}\frac{1}{M^2}\right] \qquad 4.1.1.4$$

C_γ is an empirical coefficient that provides an effective Mach number dependence for the Newtonian pressure coefficient, and is given as:

$$\begin{aligned} C_\gamma &= 1.01 + 1.31\left[\ln\left(10 M \sin\theta\right)\right]^{-7/3} && M\sin\theta \geq 0.4 \\ &= 1.625 && M\sin\theta < 0.4 \qquad 4.1.1.5 \end{aligned}$$

where θ is the angle of the body element to the incoming flow. The value for M in the above expressions is for post shock conditions, and can be written as:

$$M = M_\infty \frac{(g^*)^{\gamma + 2}}{(f^*)^{\frac{\gamma - 1}{2}}} \qquad 4.1.1.6$$

where $g^* = U/U_\infty$ is the hypersonic velocity ratio, and $f^* = \rho U^2/\rho_\infty U_\infty{}^2$ is the dynamic pressure ratio downstream of the shock. These quantities are a function of the radial position, and assuming similar profiles are themselves functions of χ^*, where χ^* is defined as:

$$\chi^* = \frac{\left(\frac{R}{d_n} - \frac{1}{2}\right)^2}{\left(\frac{R_{sh}}{d_n}\right)^2} \qquad 4.1.1.7$$

The empirical functions f^* and g^* for a blunted cone cylinder are given by:

$$f^* = f_o + 2.75\,\chi^* \qquad 4.1.1.8$$

$$g^* = 1 - 0.362\sqrt{1 - f_o} + 0.6\,\chi^{*1/2} \qquad 4.1.1.9$$

where the important parameter f_o which determines the effect of finite Mach number dependence of the profiles has been fitted to Method of Characteristics results and can be written as:

$$f_o = 0.17 + \left(\frac{9.65}{M_\infty + 8.7}\right)^3 \qquad 4.1.1.10$$

These expressions are arranged to provide close agreement with flow field calculations based on the Method of Characteristics over a wide range of Mach numbers. The maximum value of these functions cannot exceed unity at the edge of the inviscid shear layer, and are limited by this consideration to unity for $\chi^* \geq 0.302$. R_{sh} is found from

$$\frac{R_{sh}}{d_n} = K^* C_{D_n}^{1/4}\left(\frac{x - x_{sh}}{d_n}\right)^{1/2} \qquad 4.1.1.11$$

and R is given as:

$$\left(\frac{R}{d_n}\right)^2 = \left(\frac{\Delta z}{d_n}\right)^2 + 2\left(\frac{\Delta z}{d_n}\right)\left(\frac{r}{d_n}\right)\cos\alpha \sin\phi + \left(\frac{r}{d_n}\right)^2\left(\cos^2\alpha \sin^2\phi + \cos^2\phi\right) \qquad 4.1.1.12$$

where

$$\frac{\Delta z}{d_n} = \frac{x}{d_n}\sin\alpha \qquad 4.1.1.13$$

The parameter K^* in the hypersonic limit is a true constant, and has the value of unity. To incorporate the effects of Mach number we can write

$$K^* = 1 + \frac{1.57}{M_\infty^2\sqrt{C_{D_n}}}\left(\frac{x - x_{sh}}{d_n}\right) - \frac{5.80}{M_\infty^4 C_{D_n}}\left(\frac{x - x_{sh}}{d_n}\right)^2 \qquad 4.1.1.14$$

The coefficient C_{D_n} is the drag coefficient for the nose, and x_{sh} is the shock separation distance as defined in Fig. 6. The value of C_{D_n} is given as:

$$C_{D_n} = C_\gamma C_{p_{max}} \sin^2\theta_N \qquad 4.1.1.15$$

where θ_N is the nose cone half angle.

Now that the pressure distribution in the form of the pressure coefficient C_p is known, we can integrate it over the vehicle to find the net force coefficient in the normal and the axial directions. The unsteady aerodynamic characteristics of a vehicle pitching with a rate q have been investigated by Ericsson [22], who gives the final form for the integrated expressions. The results for the axial and normal forces on the body are:

$$C_A = \frac{8}{\pi\, d^2} \int_{-\frac{\pi}{2}}^{\frac{\pi}{2}} \int_{\frac{d_n}{2}}^{L} C_{p_E} \tan \theta_E \, r(x) \, dx \, d\phi \tag{4.1.1.16}$$

$$C_N = \frac{8}{\pi\, d^2} \int_{-\frac{\pi}{2}}^{\frac{\pi}{2}} \int_{\frac{d_n}{2}}^{L} C_{p_E} \cos \theta_E \sin \phi \, r(x) \, dx \, d\phi \tag{4.1.1.17}$$

Here r(x) is the local body radius and d is the maximum body diameter. The normal force derivative with respect to α can be written as:

$$C_{N_\alpha} = \frac{8}{\pi\, d^2} \int_{-\frac{\pi}{2}}^{\frac{\pi}{2}} \int_{\frac{d_n}{2}}^{L} \left[(C_{p_{\alpha L}})_1 + (C_{p_{\alpha L}})_2 + \left(\Delta^i C_{p_\alpha}\right)_2 + \left(\Delta^i C_{p_\alpha}\right)_1 \right] \cos \theta_E \sin \phi \, r(x) \, dx \, d\phi \tag{4.1.1.18}$$

In this expression the complicated function $(C_{p_{\alpha_L}})_1$ represents the pressure change caused by attitude change, $(C_{p_{\alpha_L}})_2$ is the change in blast wave pressure Cpo, $(\Delta^i C_{p_\alpha})_1$ is the pressure change on the element caused by translation of the nose in pitch, and $(\Delta^i C_{p_\alpha})_2$ is the pressure change on the element due to the effective shape change of the nose tip in pitch. These are given in Appendix B. The normal coefficient derivative is required in order to determine the stability characteristics of the vehicle.

4.1.2 Stability Coefficients and Moments

The static and dynamic pitching and yawing moment coefficients may be written as follows. The pitch moment coefficient is:

$$C_m = -\frac{8}{\pi d^3} \int_{-\frac{\pi}{2}}^{\frac{\pi}{2}} \int_{\frac{d_n}{2}}^{L} C_{p_E} \cos \theta_E \sin \phi \, r(x) \left(x - x_{CG} + r(x) \tan \theta_E \right) dx \, d\phi$$

4.1.2.1

and its derivative with respect to α can be written:

$$C_{m_\alpha} = -\frac{8}{\pi d^3} \int_{-\frac{\pi}{2}}^{\frac{\pi}{2}} \int_{\frac{d_n}{2}}^{L} \left[(C_{p_{\alpha L}})_1 + (C_{p_{\alpha L}})_2 + \left(\Delta^i C_{p_\alpha}\right)_2 + \left(\Delta^i C_{p_\alpha}\right)_1 \right]$$

$$\left(x - x_{CG} + r(x) \tan \theta_E \right) \sin \phi \, r(x) \, dx \, d\phi$$

4.1.2.2

Here pitch and yaw are interchangeable given the axisymmetric formulation of the problem, and we would simply use the yaw angle for determining the force and moment coefficients in the plane of yaw.

The total dynamic damping derivative may be written:

$$C_{m_q} + C_{m_{\dot{\alpha}}} = -\frac{8}{\pi d^3} \int_{-\frac{\pi}{2}}^{\frac{\pi}{2}} \int_{\frac{d_n}{2}}^{L} \left[(C_{p_q})_1 + (C_{p_q})_2 + \left(\Delta^i C_{p_{\dot{\alpha}}}\right)_2 + \left(\Delta^i C_{p_{\dot{\alpha}}}\right)_1 \right]$$

$$\left(x - x_{CG} + r(x) \tan \theta_E \right) \sin \phi \, r(x) \, dx \, d\phi$$

4.1.2.3

The quantities subscripted by q denote the damping due to the pitching motion, and the subscript α denotes the dynamic damping contribution which is generated by convective time lag effects due to the changing angle of attack. These functions are given in Appendix B.

The equations above constitute the complement of forces and moments due to the pressure distribution about the vehicle that are needed for the solution of the equations of motion.

4.2 Viscous Forces and Moments

The shear stresses on the fluid particles give rise to drag forces in the form of skin friction, and Magnus forces due to the asymmetric boundary layer about the vehicle, caused by its spinning. Further, the addition of mass into the boundary layer caused by the ablation process may result in a significant net side force in the plane of yaw. These forces and the moments they generate will be discussed in this section.

4.2.1 Magnus Force and Moment

The Magnus force acting on the vehicle is due to the pressure difference on either side of it. This gives rise to a force in the plane of yaw. Following the analysis of Vaugn and Reiss [31] for a laminar boundary layer, the technique is extended here to turbulent boundary layers and includes a velocity correction term suggested by Vaugn and Reiss to take into account the effects of nose blunting. The contribution of the skin friction variation in the circumferential direction is implicitly assumed in the theory.

The pressure difference across the body can be written for the conical forebody as:

$$[P_1 - P_2] = \frac{h}{2} \rho_\infty r_b p \left(2 V_\infty \sin\alpha \sin\phi\right) \frac{\delta_n}{r_b} \qquad 0 \le \phi \le \pi \qquad 4.2.1.1$$

and for the cylindrical after body as:

$$[P_1 - P_2] = \frac{h}{2} \rho_\infty r_b p \left(3 V_\infty \sin\alpha \sin\phi\right) \frac{\delta_a}{r_b} \qquad 0 \le \phi \le \frac{\pi}{2}$$

$$[P_1 - P_2] = \frac{h}{2} \rho_\infty r_b p \left(3 V_\infty \sin\alpha \left(\sin\phi + |\alpha| \left[4.05 \sin 2\phi + 1.15 \sin 4\phi\right]\right)\right) \frac{\delta_a}{r_b} \qquad \frac{\pi}{2} \le \phi \le \pi$$

4.2.1.2

where h is defined as:

$$h = 1.3\left(\frac{T_\infty}{T'}\right) + 0.04 + \left[\,1 - 0.23\left(\frac{p\,d}{2\,V_\infty}\right)^2 L^2 + 0.0159\left(\frac{p\,d}{2\,V_\infty}\right)^4 L^4\right]\frac{1.24}{\sqrt{\left|1 - M_\infty^2\right|}} \qquad 4.2.1.3$$

and T'/T∞ is the compressibility correction term that is given by Eckert [35] for turbulent flow as:

$$\frac{T'}{T_\infty} = 1 + 0.037\,M_e^2 + 0.5\left(\frac{T_w}{T_\infty} - 1\right) \qquad 4.2.1.4$$

The Mach number M_e is that at the outer edge of the boundary layer. The boundary layer thickness δ used in the above expressions is simply that for turbulent boundary layers and is:

$$\delta_n = \frac{0.37\,x}{\sqrt{3}\,Re_x^{1/5}}\left(\frac{T'}{T_\infty}\right)\frac{V_c}{V_\infty}$$

$$\delta_a = \frac{0.37\,x}{Re_x^{1/5}}\left(\frac{T'}{T_\infty}\right) \qquad 4.2.1.5$$

where the term V_c/V_∞ takes into account any blunting of the nose, and the square root of three in the denominator for the cone boundary layer expression comes from the Mangler transformation [31].

If we integrate the pressure difference across the body over the vehicle surface area we can find the total Magnus force, and if the Magnus force coefficient is defined to be:

$$C_{y_{p\alpha}} = \frac{F_y}{\frac{1}{2}\,\rho_\infty V_\infty^2\left(\frac{p\,d}{2\,V_\infty}\right)\frac{\pi\,d^2}{4}\,\alpha} \qquad 4.2.1.6$$

then the Magnus force coefficient is:

$$C_{Y_{p\alpha}} = -1.233\, h \left(\frac{T'}{T_\infty}\right)(1 - 1.52\, |\alpha|)\frac{L_1^2}{Re_{L_1}^{1/5}}\left[1 - \left[1 - \frac{0.284}{(1 - 1.52\, |\alpha|)}\right]\left(\frac{L_c}{L_1}\right)^{9/5}\right] \tag{4.2.1.7}$$

The Magnus moment coefficient can be written as:

$$C_{N_{p\alpha}} = -0.793\, h \left(\frac{T'}{T_\infty}\right)(1 - 1.52\, |\alpha|)\frac{L_1^3}{Re_{L_1}^{1/5}}\left[1 - \left[1 - \frac{0.866}{(1 - 1.52\, |\alpha|)}\right]\left(\frac{L_c}{L_1}\right)^{14/5}\right] + \frac{x_{CG}}{d}\, C_{Y_{p\alpha}} \tag{4.2.1.8}$$

where the moment is taken about the vehicle center of mass. It should be noted that the Magnus force does not act through the center of pressure and its moment arm is given by dividing Equation 4.2.1.8 above by Equation 4.2.1.7.

Chapter 5

Heat Transfer Effects

Because of the high velocity of the vehicle, it will undergo severe aerodynamic heating, both convective and radiative. The effect of ablation on the vehicle is to change its aerodynamic characteristics due to the blunting of the vehicle nose, both with regards to the drag coefficient through shape change and also with regards to the stability due to the side force created. Because of the extremely high Mach number of the cases being considered the radiative heating of the blunted nosecone cannot be entirely neglected. The purpose of the heat transfer analysis performed is in consideration of possible effects on vehicle stability, and is therefore elementary. If much blunting of the nosetip occurs, or if the mass addition due to ablation is high, it can change the stability characteristics of the vehicle.

At the extremely high temperatures behind the shock, on the order of 14,000 ^{o}K, the real gas effects of air have to be included in the analysis and the ideal gas shock jump conditions are not valid. In order to find the temperature behind the shock, an empirical correlation formulated by Park and Bowen [36] from enthalpy considerations is used, and has been modified to improve its accuracy for the lower temperature range of current conditions.

The heat transfer is calculated assuming a fully turbulent flow except within the immediate region of the stagnation point, where the flow is laminar. The heat transfer is found for mass injection into the boundary layer of a high temperature graphite ablator. The mass loss is assumed to occur only at the tip, and sidewall ablation is considered negligible. This is a good approximation, as indicated by the experimental results of Wilkins and Tauber [37] for velocities up to 7.3 km/sec. In addition, the effects of convective and radiative heating are considered independent for the purpose of the analysis, even though they are interdependent as will be discussed Chapter 7.

5.1 Convective Heating

For heat transfer rates to the stagnation point of the body for wall temperatures below approximately 4000 ^{o}K in the flight regime where $1000 \leq U_{\infty} \leq 10000$ m/sec we can write from Tauber [38]:

$$\dot{q}_{x_s} = 1.83\left(10^{-4}\right)\left(\frac{\rho_{\infty}}{r_n}\right)^{1/2} U_{\infty}^{3}\left(1 - \frac{h_w}{H_s}\right) \qquad 5.1.1$$

This result is for a laminar, cold wall, with no mass addition at the stagnation point. This implies that the influence of the wall affects the heating through the temperature of the wall only. This is a good assumption for an ablating surface since the wall temperature is the temperature at which mass is removed from the surface, and is always the temperature at which the surface ablates. This expression is independent of wall temperature, and is valid for cases where $h_{\infty} << U_{\infty}^{2}$. The value of h_W is the static enthalpy at the wall, and H_S is the total enthalpy at the stagnation region.

When the flow over the stagnation region is laminar, studies have shown that the heat transfer rate over the blunted nose can be approximated using the cosine law, which even though empirical has a theoretical basis for angles up to 45^{o}. We can write:

$$\frac{\dot{q}_w}{\dot{q}_{w_s}} = \cos\lambda \qquad 5.1.2$$

where λ is the body angle given by x/r. This expression is approximately accurate for angles up to 75^{o} [38]. The tangency point of the cone to the spherical cap is 80^{o} for a 10^{o} nose-cone, and this expression is therefore assumed valid to this location. Then the heat transfer to the body can be approximated as the stagnation point value multiplied by the crossectional area of the blunted nose. The cosine distribution will be modified due to the onset of turbulence almost immediately off the stagnation point, but the change due to turbulence is small for extreme environments [36].

If we want to include the effects of a high temperature ablator such as carbon-carbon we have to take into account the mass addition into the turbulent boundary layer and the effects of the chemical reactions between the injected species and the air. The effects of turbulence are accounted for semi-empirically in the method of Putz and Bartlett [39]. We can take these factors into account by defining a function φ such that:

$$\varphi = \frac{\dot{q}_w}{\dot{q}_{wB=0}} \qquad 5.1.3$$

where B is defined to be the mass addition parameter

$$B = \frac{\dot{m}_w}{\dot{q}_{wB=0}}(H_e - h_w) \qquad 5.1.4$$

and m_w is the mass addition rate. Here H_e is the total enthalpy at the edge of the boundary layer, and is approximated by H_s. Putz and Bartlett derived the empirical relation for the ablating surface as:

$$\varphi' = 1 - a\,B + b\,B^2 + c\,B^3 - d\,B^4 \qquad 5.1.5$$

where a = 0.6563, b = 0.01794, c = 0.06365, and d = 0.01125. Here φ' is defined as:

$$\varphi = \varphi' + \frac{\left(\frac{\Delta H_c}{H_e}\right)}{\left(1 - \frac{h_w}{H_e}\right)} \qquad 5.1.6$$

The ratio $\Delta H_c/H_e$ accounts for the gas phase chemical reactions and diffusion effects for injected species, and its value is found from Putz and Bartlett [39] for graphite based ablators with a given mass addition parameter.

5.2 Radiative Heating

At the extremely high velocities in question here, where the temperature of the air behind the shock is large, we have to include the effects of radiative heat transfer. This cannot be neglected, as the radiative heating rate goes as the fourth power of temperature and may be significant. According to Park and Bowen [36] the dominant form of heat transfer may be radiation, since as the layer of ablation gases is formed it will block the effects of convection and diffusion. Fig. 7 shows the stagnation region for the analysis of radiative heating. The radiation reaching the wall is diminished by the layer of gases due to its opacity. Park and Bowen have assumed an optically thick Rosseland approximation which is valid at the high pressures of the lower altitudes. As the altitude is increased, it overestimates the heat transfer rate as the Rosseland approximation becomes less valid.

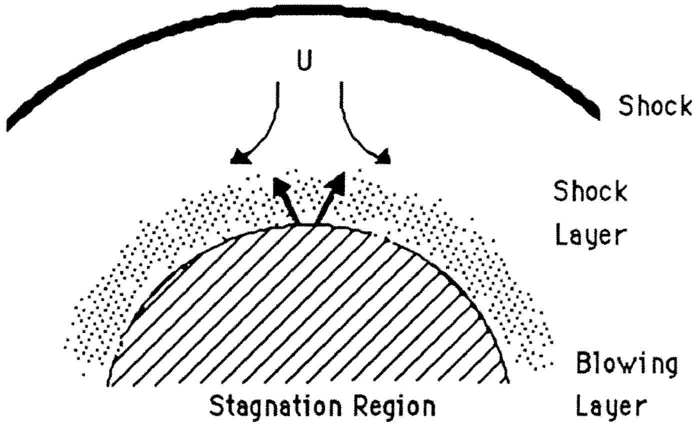

Figure 7. The Ablating Surface of a Hypersonic Blunt Body

The approach employed here is the method of Probstein [40], who uses the radiation conduction equation valid for optically thick media and a radiation 'slip condition'. He derives an equation of the form:

$$q_w = \frac{\sigma\left(T^4 - T_w^4\right)}{1 + \frac{3\tau}{4}} \qquad 5.2.1$$

Here τ is defined as $\tau = \Delta / l_v$, where Δ is a characteristic length which in the current problem is the shock detachment distance, and l_v is the photon mean free path, or the inverse of the absorption coefficient. For large and small τ Equation 5.2.1 takes on the correct limiting values. The value for the mean opacity is found from an empirical correlation given by Park and Bowen as:

$$\alpha = \alpha_r\left(\frac{\rho}{\rho_r}\right)\left(\frac{p}{p_r}\right)^{1/2}\left(\frac{T}{10000}\right)^{2.5} \qquad 5.2.2$$

Here p, ρ, and T are after shock conditions, and the reference values are at sea level. This expression with $\alpha_r = 0.16\ \mathrm{cm}^{-1}$ yields approximate values for the Rosseland mean free path $1/\alpha$,which correspond to experimentally found values for a carbon gas layer at high pressures. The post shock temperature can be found from enthalpy considerations and the empirical relationships:

$$H = H_r\left(\frac{T}{8000}\right)^{1.5}$$

$$H_r = 3.6 \times 10^7\left(1 - \frac{1}{6}\log\left(\frac{p}{100}\right)\right) \qquad 5.2.3$$

Here p is the stagnation pressure in atmospheres, and H is in J/kg. The equation is slightly modified from that of Park and Bowen to better fit the lower temperature range of this study. This expression, when used for finding the post shock temperature at initial launch, yielded an error in T^4 of only 13% for black body radiation when compared to the temperature found from Mollier chart diagrams [41], thus the radiative heat transfer to the surface can be approximated using the preceding equations for all altitudes since it would be the conservative estimate.

Chapter 6

Stability Requirements

Since the exact equations of motion are being solved in their complete form a detailed stability analysis is not performed. Rather if the solution to the equations of motion does not diverge, then the motion is considered stable. It is sometimes necessary, hoever, to have an approximate set of constraints that bound the solution. For the case where the pitch moment derivative is positive it is required that certain stability constraints be met [42]. It is these formulations that are presented here.

6.1 Gyroscopic Stability

The most important stability condition is that given by the gyroscopic stability factor. If this condition is not met then the gyroscopic forces are unable to balance the aerodynamic forces and the vehicle will be unstable. It is essentially a function of the spin rate, and may be written as:

$$S_g = \frac{2\, I_x^2\, p^2}{\pi\, d^3\, \rho\, U^2\, C_{m_\alpha}\, I_y} \qquad 6.1.1$$

It is the ratio of squared gyroscopic spin to the static moment coefficient. When this factor is greater than unity periodic motion occurs and the vehicle will be gyroscopically stable. From this we can determine the minimum rate of spin that the vehicle must have in order to be statically stable.

6.2 Dynamic Stability

The dynamic stability factor is essentially the ratio of the Magnus moment coefficient to the damping moment coefficient, and it can be written:

$$S_d = \frac{2\left(C_{N_\alpha} - C_D + \frac{m\,d^2}{2\,I_x} C_{N_{p\alpha}} \right)}{\left(C_{N_\alpha} - C_D - \frac{m\,d^2}{2\,I_y} C_{m_q} \right)} \qquad 6.2.1$$

The limits of the dynamic stability factor are $0 \leq S_d \leq 2$, and any vehicle lying outside this range will not be dynamically stable. The dynamic stability factor is primarily a function of vehicle configuration.

6.3 Further Conditions on Stability

In addition to satisfying the stability factors individually, a dynamically stable vehicle must satisfy the condition:

$$S_g \geq \frac{1}{S_d(2 - S_d)} \qquad (23)$$

The implications of these conditions are that any vehicle can be made gyroscopically stable with sufficient spin, but that this does not necessarily imply that the vehicle will be stable. A dynamically stable vehicle must also be statically stable, and if the dynamic stability factor lies inside the allowed range $0 \leq S_d \leq 2$, then a statically unstable vehicle can be made stable with a sufficiently high rate of spin. When the dynamic stability factor is outside this range, then a statically unstable vehicle cannot be spin-stabilized and a statically stable vehicle may be made dynamically unstable by too high a rate of spin. Thus, certain vehicle configurations cannot be made stable by spinning.

Chapter 7

Results and Discussion

The analyses of Chapters 4 and 5 are carried out for the initial configuration of the ram accelerator vehicle, and then the equations of motion of Chapter 2 are solved numerically in order to determine the flight path characteristics. At each time step new aerodynamic coefficients are found for the vehicle configuration. This is required since as the vehicle transits the atmosphere, its attitude, and therefore its aerodynamic coefficients, change with time.

7.1 Results

7.1.1 Results of the Aerodynamic Force Calculations

The methods of Chapter 4 and 5 were applied to the ram accelerator mass launch vehicle and the results of the analysis are presented in Figures 8-15 for sideslip angles of $\beta = 0^{o}$. The initial configuration of the ram accelerator vehicle is:

$d_n/d=0.13$

$L/d=10.0$

$x_{cg}/L=0.70$

$M_\infty=30.0$

Figure 8 shows the pressure distribution C_{p_E} about the nose cone and the shoulder region at an angle of attack of $\alpha = 2^{o}$ for the windward and the leeward side of the vehicle as a function of position. Although not shown for clarity, the pressure coefficient at the stagnation point reaches its maximum value of 2.6 and decreases rapidly as it expands over the spherical nose tip. There is an over-expansion region as the flow accelerates about the tip, and then the pressure recovers as the flow is compressed by the conical forebody. There is a rapid

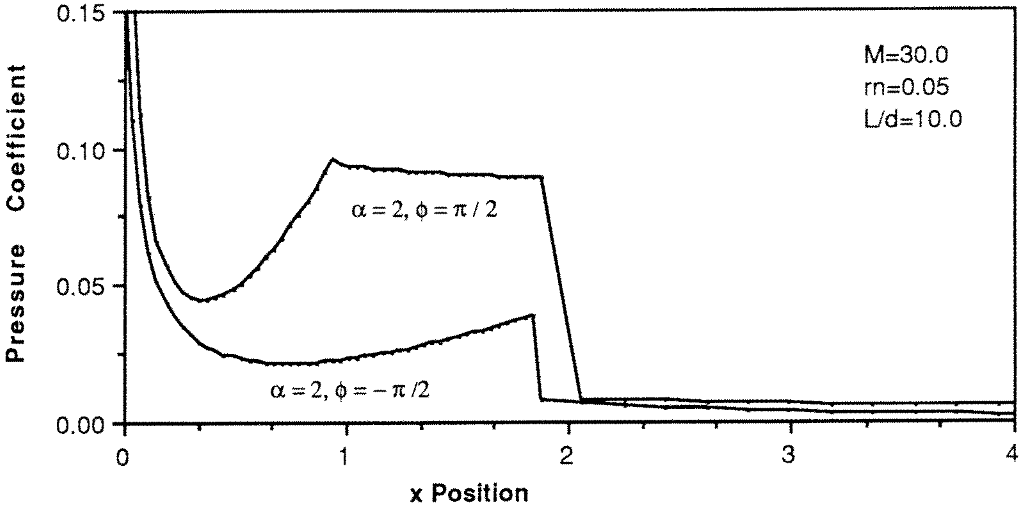

Figure 8. Pressure Coefficient vs. Axial Position on Vehicle

expansion at the vehicle shoulder, followed by a slowly decreasing pressure gradient over the cylindrical afterbody. The effect of such a pressure gradient is to induce a lift force on the body, and as can be seen, it is concentrated in the forebody region, which gives rise to large moments about the vehicle center of mass.

Figure 9 shows the variation of the axial force coefficient C_A and the normal force coefficient C_N with angle of attack due to the increasing pressure force on the windward side of the vehicle. This is indicative of very high Mach number flows, where C_A is essentially invariant, and C_N increases steadily with increasing angle of attack. The effects of the normal force are to create a pitching moment about the vehicle center of mass, as shown in Fig. 10. The pitching moment increases rapidly with angle of attack, although this increase is essentially linear, as shown in Fig. 11, where the pitch moment derivative C_{m_α} is shown with respect to the pitch angle. The effect of a positive pitching moment is to destabilize the vehicle, and any increase in angle of attack will only cause it to increase further. The total pitch damping derivative C_{m_θ} is shown in Fig. 12, and it can be seen that it is quite large, $C_{m_\theta} = -45$, due to the length of the afterbody.

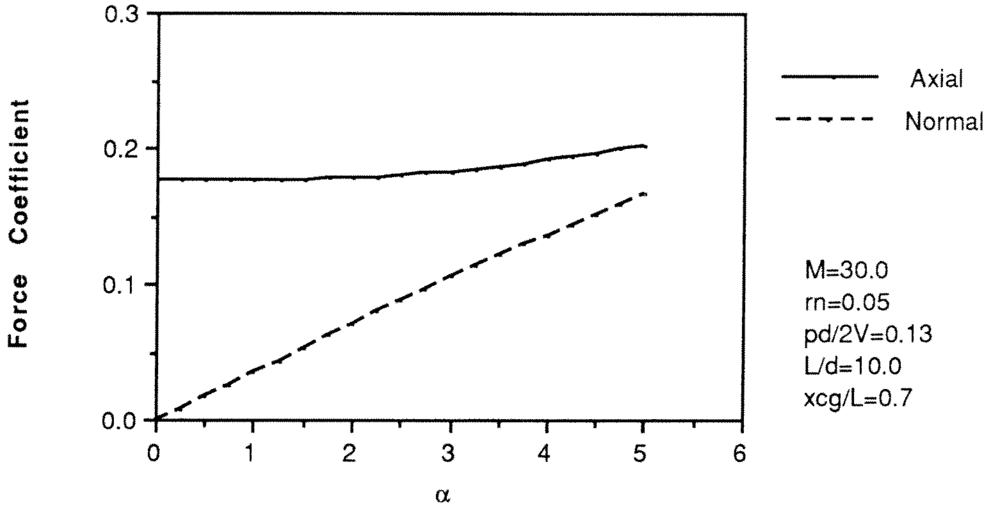

Figure 9. Axial and Normal Forces for the Ram Accelerator Vehicle

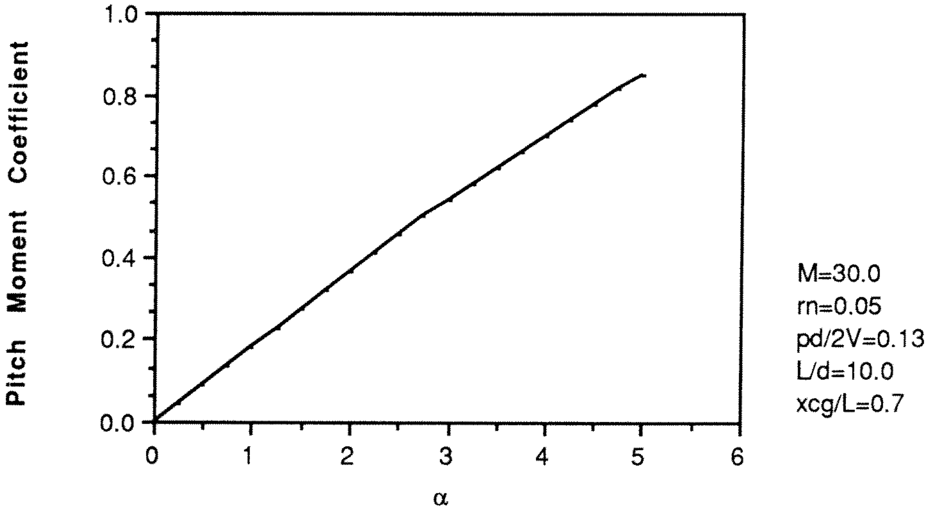

Figure 10. Pitch Moment Coefficient for the Ram Accelerator Vehicle

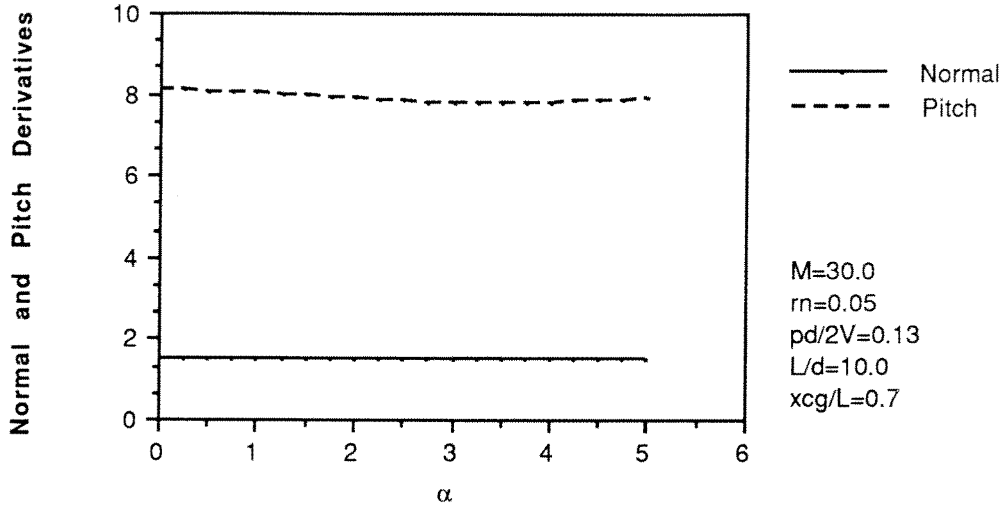

Figure 11. Normal and Pitch Derivatives for the Ram Accelerator Vehicle

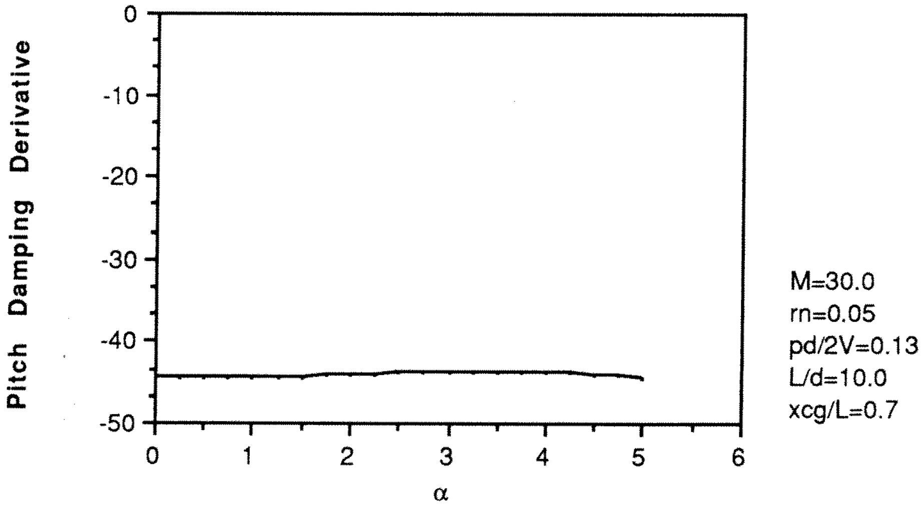

Figure 12. Pitch Damping Derivative for the Ram Accelerator

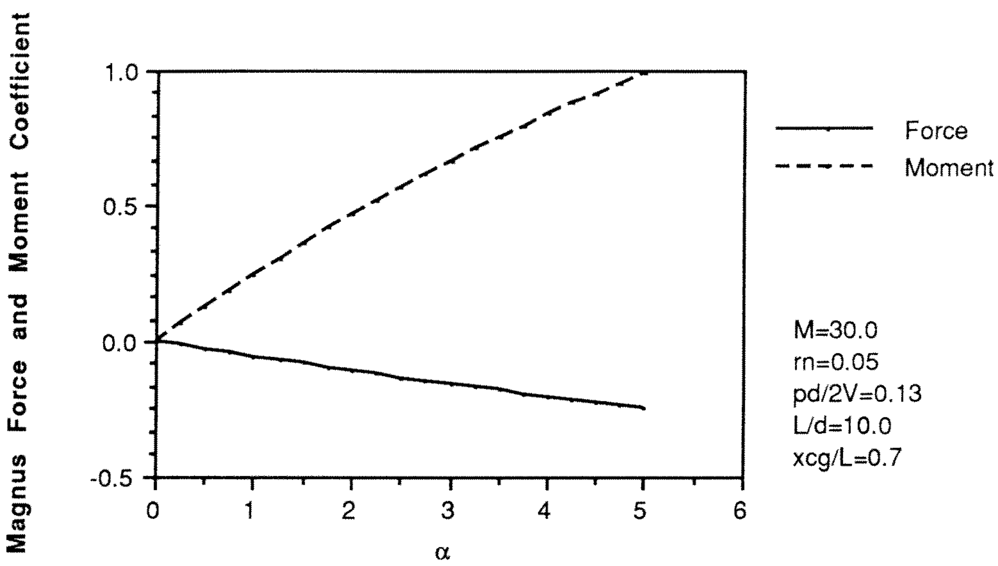

Figure 13. Magnus Force and Moment Coefficient for the Ram Accelerator

The Magnus force C_{Y_p} and moment coefficients C_{N_p} are shown in Fig. 13, and are quite large. This is characteristic of highly spun hypersonic vehicles. The Magnus force is in the negative direction in the plane of yaw and creates a positive moment. Figures 14 and 15 show the relative magnitudes of the forces and moments acting on the vehicle. The largest force is naturally the drag force, but as the angle of attack increases the vehicle normal force approaches it in magnitude. The Magnus force is approximately 1/5 the normal force over most of the range of angles of attack . The relative magnitude of the moments created by these forces is shown in Fig. 15, and it can be seen that the pitch moment is indeed the largest and that it therefore merits the most consideration in stability analyses.

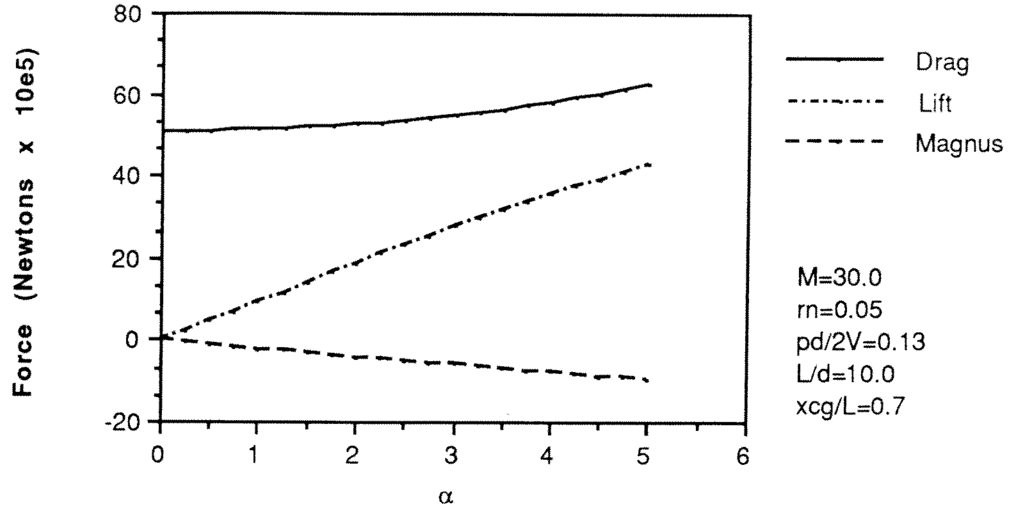

Figure 14. Relative Magnitude of Forces for the Ram Accelerator Vehicle

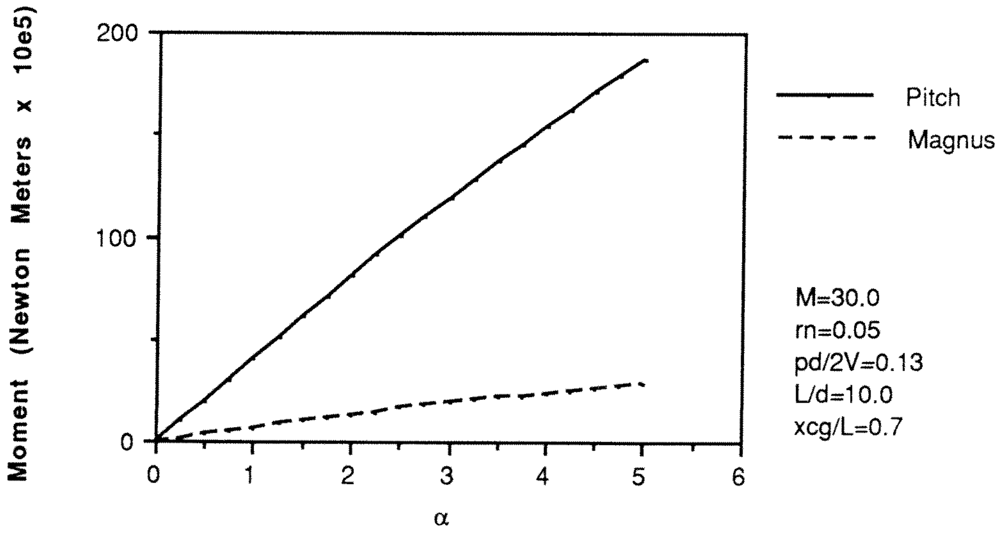

Figure 15. Relative Magnitude of Moments for the Ram Accelerator Vehicle

7.1.2 Solutions for the Equations of Motion

The test of vehicle stability is the solution of the equations of motion. It is found that the given initial configuration of the ram accelerator vehicle is dynamically unstable, and the equations of motion diverge rapidly and cannot be solved. The effects are so large that the vehicle begins to tumble within a few iterations of the initial conditions, and the solution of the equations of motion in such a case is of no practical value. When the stability conditions of Chapter 6 are applied, it is evident that the vehicle is highly unstable, and indeed cannot be spin stabilized in its current configuration.

If the results for the aerodynamic force coefficients are substituted into the stability criteria for gyroscopic and dynamic stability we see that the stability factors are well outside their limits. At an angle of attack of 1° the gyroscopic stability factor for the ram accelerator vehicle is approximately $S_g = 0.05$. Given a high enough spin rate the vehicle can be made gyroscopically stable, and at an angle of attack of 1° the spin rate required is approximately 17,000 rad/sec. This, however, does not guarantee stability as the conditions for the dynamic stability factor must also be satisfied. The dynamic stability factor for the ram accelerator vehicle at 1° angle of attack is $S_d = 37.4$, well outside the limits $0 \leq S_d \leq 2$. This implies that the current configuration of the ram accelerator vehicle cannot be spin stabilized under any conditions.

From the form of the dynamic stability factor it can be seen that the destabilizing term is the Magnus moment derivative. From the results presented previously in Figures 9 and 11 the normal coefficient derivative and the drag coefficient are essentially constant over the small range of angles of attack being considered. If their values at 1° angle of attack are assumed, then in order for the dynamic stability factor to satisfy its constraints the Magnus moment derivative is required to be $C_{N_{P\alpha}} \leq 0.87$. This represents a reduction of the allowable Magnus moment by a factor of 20 over what has been calculated.

The considerations for a more stable vehicle design are discussed in Section 7.3, where based upon a new vehicle configuration, the stability factors may be met and then the equations of motion may be solved. The effects of various changes of vehicle configuration and how they affect the aerodynamic coefficients, and hence the stability factors, will be discussed in Section 7.2.

7.1.3 Heat Transfer Calculations

In view of the above stability considerations, the heat transfer analysis for the ram accelerator vehicle was performed by forcing the vehicle to be stable-i.e. the angle of attack was set to zero. This gives no destabilizing forces or moments and atmospheric transit can be assured. For an initial launch velocity of 10,000 m/sec at sea level, and a flight path angle of 20^0, the vehicle retained 65% of its initial velocity, and almost the entire velocity loss occured below 18,000 m.

The results of the analysis are presented in Figures 16-19 for the stagnation region. It can be seen that the radiative heat transfer cannot be entirely neglected. Fig. 16 shows the relative magnitudes of the convective heating to the body with and without ablation. At the higher altitude the two lines converge since the mass injection into the boundary layer becomes small, and the effects of the reduction of convective heat transfer caused by the ablation process are no longer important. The peak heating rate is 14.5 kW / cm^2 and occurs at 4000 m. Although this is high, it decreases rapidly with altitude and at 24,000 m it is only 4.8 kW / cm^2, less than 1/3 of its peak value.

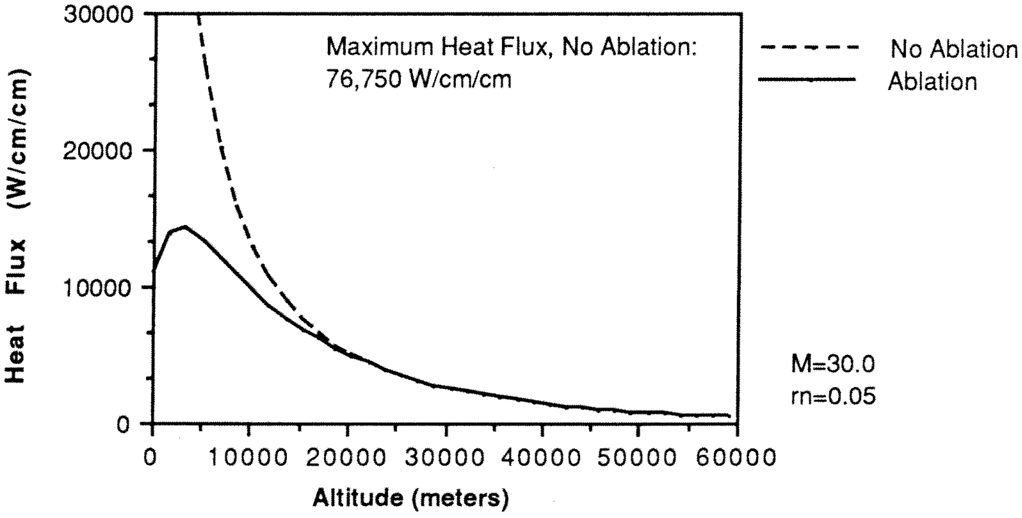

Figure 16. Effects of Ablation on Convective Heat Transfer

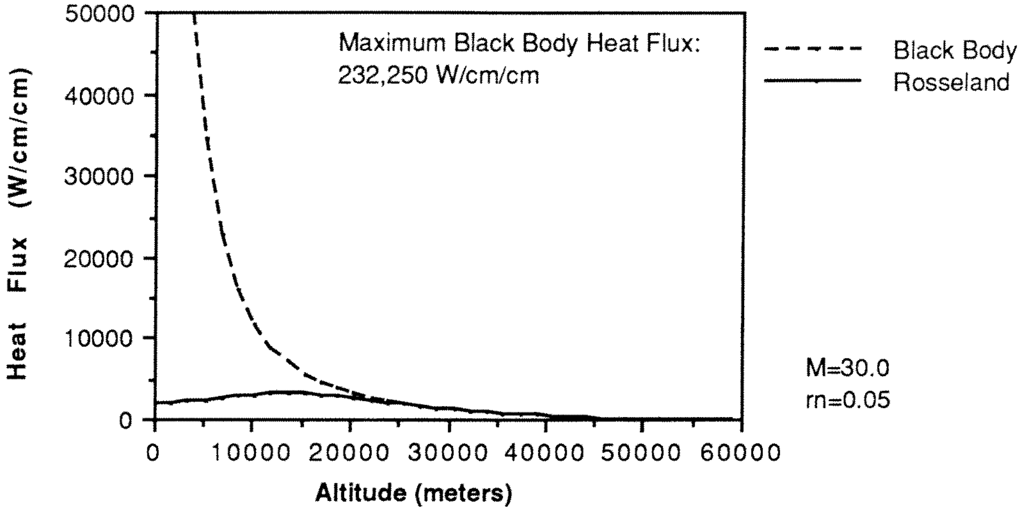

Figure 17. Effects of Ablation on Radiative Heat Transfer

The radiative heating effects are shown in Fig. 17, where the radiative heat transfer to the vehicle is shown with the black body limit as a comparison. At the lower altitudes the radiative heat transfer to the vehicle is greatly reduced due to the optical thickness of the ablative layer. As density and mass loss decrease with increasing altitude, the opacity of the blowing layer decreases and more of the radiation reaches the surface of the vehicle. The peak heating rate is 4 kW / cm^2 and occurs at 14,000 m. The peak radiation rate occurs at this rather high altitude primarily because the model tends to overpredict the radiation effects at the higher altitudes.

Figure 18 shows the relative magnitude of the convective and radiative contributions to the overall heating rate. It can be seen that for the entire altitude range the convective effects dominate. It should be pointed out that the radiative heat transfer to the vehicle is overestimated at the upper altitudes using this model, but due to the low overall mass loss its conservative results are sufficient for the present analysis

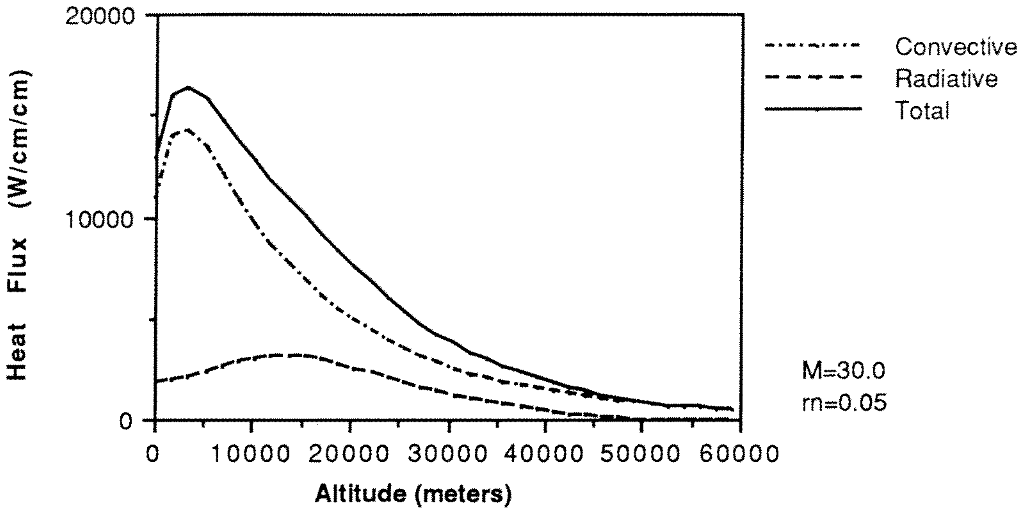

Figure 18. Convective and Radiative Heating Contributions

Fig. 19 shows the total mass loss of the vehicle with altitude, and it is shown that it amounts to only 2.0 kg. The contribution of convection is 1.6 kg, and that of radiation is 0.4 kg. Most of the mass loss occurs at altitudes below 20,000 m and represents only 0.1% of the overall vehicle mass.

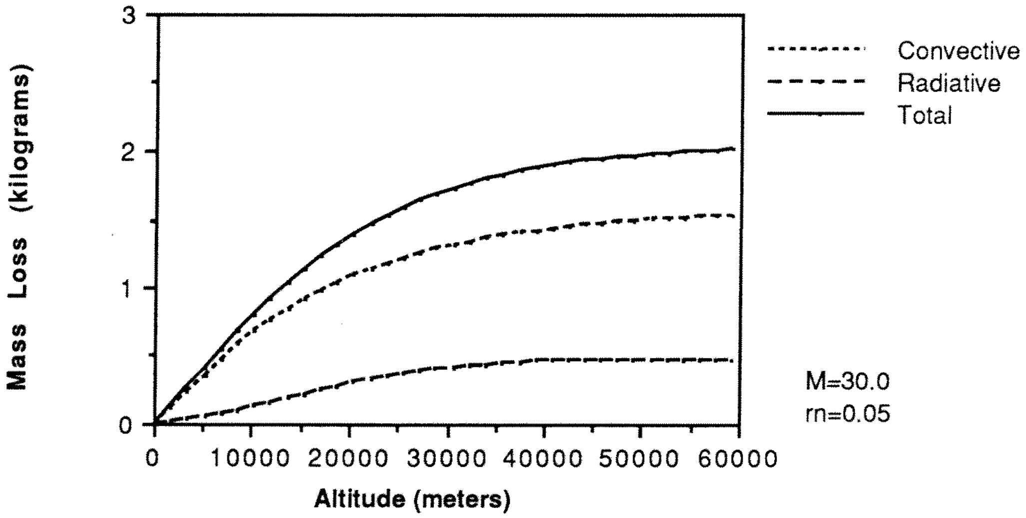

Figure 19. Mass Loss During Atmospheric Transit of Ram Accelerator

The extremely low mass loss implies that the mass injection into the boundary layer is not significant in terms of the stability considerations discussed previously in Chapter 3, and the nose bluntness increases to less than $r_n/r_b = 0.15$ from the initial configuration of $r_n/r_b = 0.13$. Since the mass loss is small and the nose radius does not change greatly, the effects of ablation do not significantly affect the stability of the vehicle. The coupled effects of radiation and convection are discussed in Section 7.2.6.

7.2 Discussion

The important variable parameters of the problem are the Mach number, the bluntness ratio of the nose, d_n/d, the length of the vehicle, L/d, and the position of the center of gravity, x_{cg}/L. The effect of varying any one of these values can significantly alter the magnitude of the coefficients, and hence the stability of the equations of motion. How a change in each of these quantities affects the aerodynamic characteristics is presented below, with a discussion of its effects on stability. As each indicated vehicle variation is performed, the other vehicle parameters are kept constant.

7.2.1 Mach Number Variation

The effects of Mach number variation on the aerodynamic characteristics for the ram accelerator vehicle configuration are shown in Figures 20-24 for angles of attack of 1° and 2°. Figure 20 shows the axial drag coefficient C_A which decreases with increasing Mach number to $C_A = 0.17$, and then remains essentially constant. This is characteristic of hypersonic drag profiles.

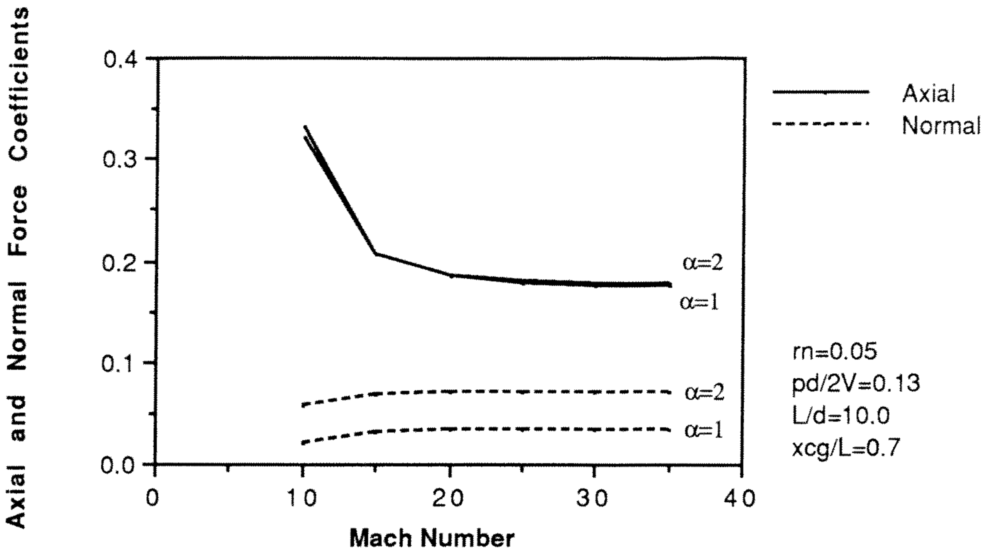

Figure 20. Axial and Normal Force Coefficients for Varying Mach Number

The normal coefficient C_N is essentially constant over the Mach number range of interest, but it increases slightly with increasing Mach number due to the higher pressure forces on the winward side of the vehicle. Fig. 21 shows the pitch moment coefficient C_m which increases with Mach number and then levels off to a constant value. It is also shown in these figures that at high Mach numbers the normal force coefficient and pitch moment are strong functions of angle of attack.

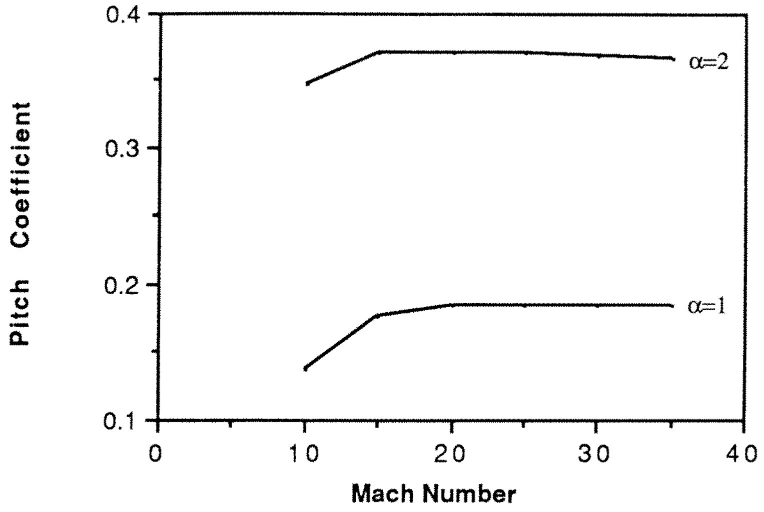

Figure 21. Pitching Moment Coefficient for Varying Mach Number

The Magnus force and moment coefficients C_{Y_p} and C_{N_p} are shown in Fig. 22, and increase with increasing Mach number.

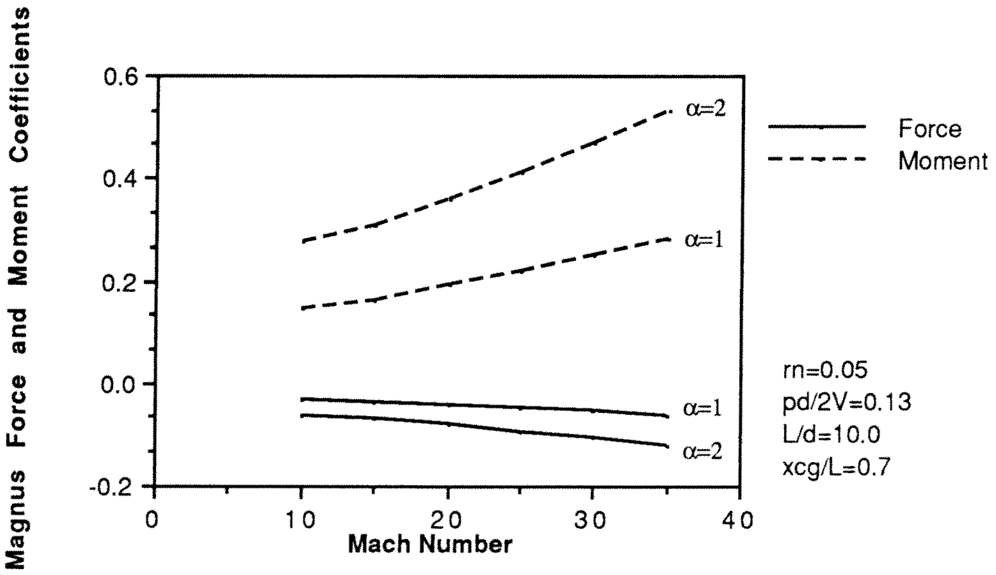

Figure 22. Magnus Force and Moment Coefficients for Varying Mach Number

Figures 23 and 24 show the normal and pitch derivatives $C_{N\alpha}$ and $C_{m\alpha}$, and the pitch damping derivative $C_{m\theta}$. The normal derivative does not vary much over the Mach number range, but the pitch and pitch damping derivatives are strong functions of Mach number. The pitch derivative increases steadily until $M_\infty = 20$, and then remains essentially constant.

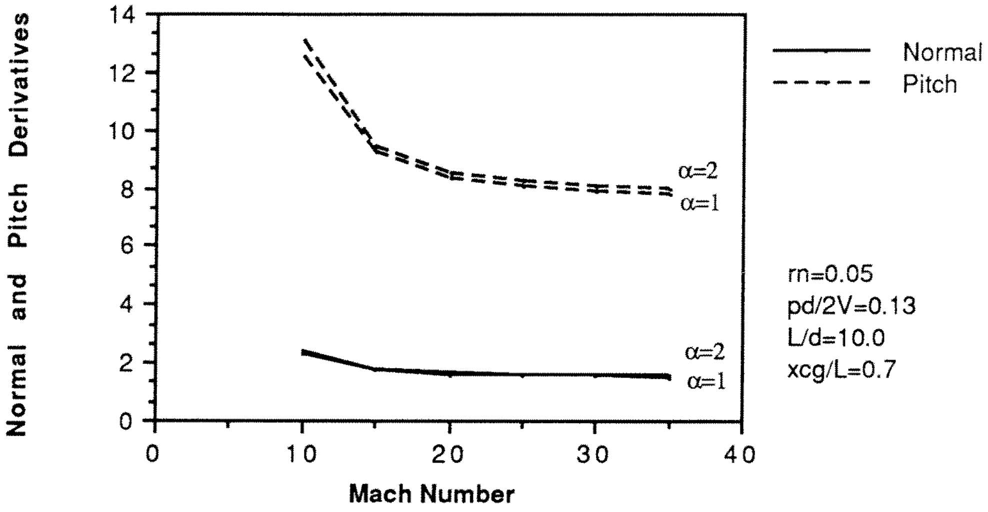

Figure 23. Normal and Pitch Derivatives for Varying Mach Mumber

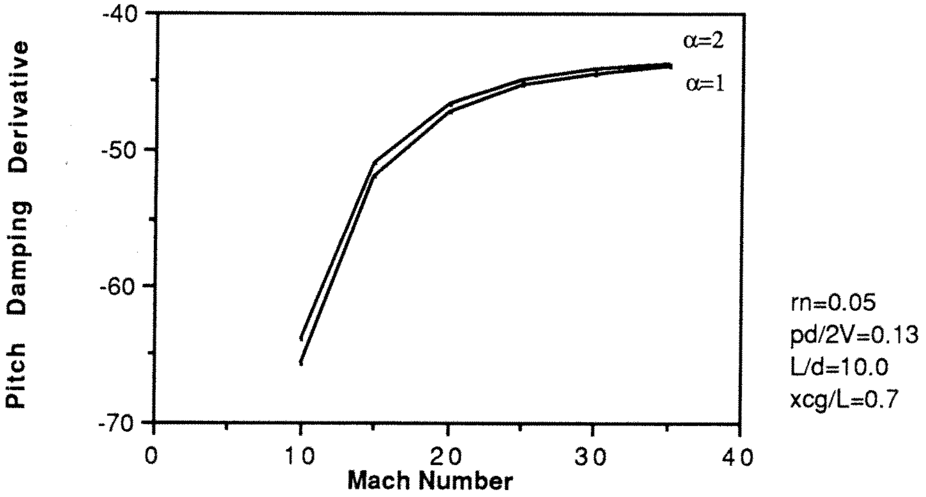

Figure 24. Pitch Damping Derivative for Varying Mach Number

7.2.2 Nose Bluntness Variation

The effects of nose bluntness are quite pronounced, as is shown in Figures 25-29. The most dramatic effects are at the higher angles of attack. Fig. 25 shows the axial and normal force coefficients C_A and C_N, and the effects of nose blunting are to dramatically increase the axial drag and to substantially decrease the normal lifting force. The axial drag coefficient for $r_n/d = 0.4$ is approximately 1.5 times that for $r_n/r_b = 0.1$. The normal force coefficient is also a strong function of nose bluntness, especially at the higher angles of attack, where the $r_n/r_b = 0.4$ case provides only 1/3 the normal force of the $r_n/r_b = 0.1$ case. This is further reflected in Fig. 26, which shows the pitch coefficient C_m. Since the normal force is reduced for blunted bodies the moment created about the vehicle center of mass also decreases with increasing nose bluntness, and therefore nose blunting contributes to increased static stability.

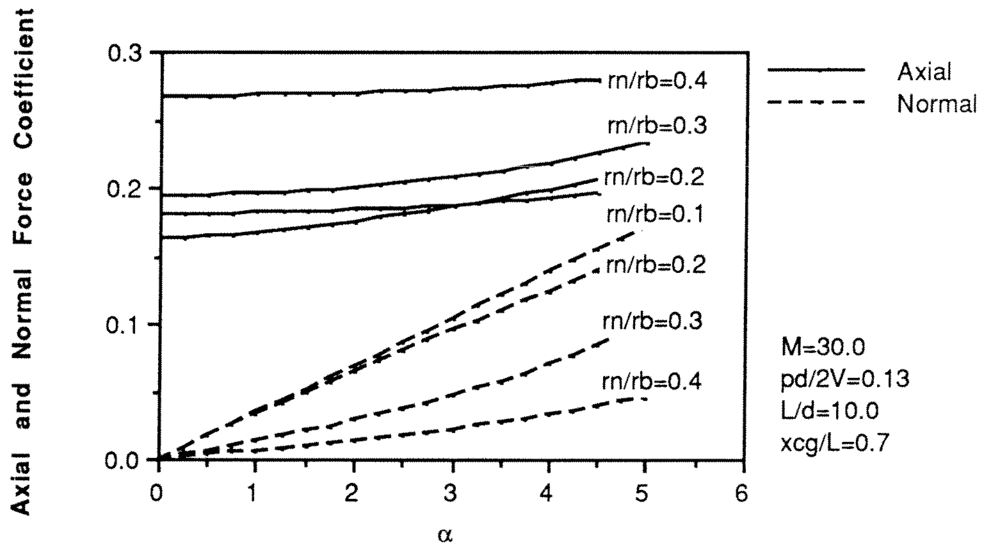

Figure 25. Axial and Normal Force Coefficients for Varying r_n/r_b

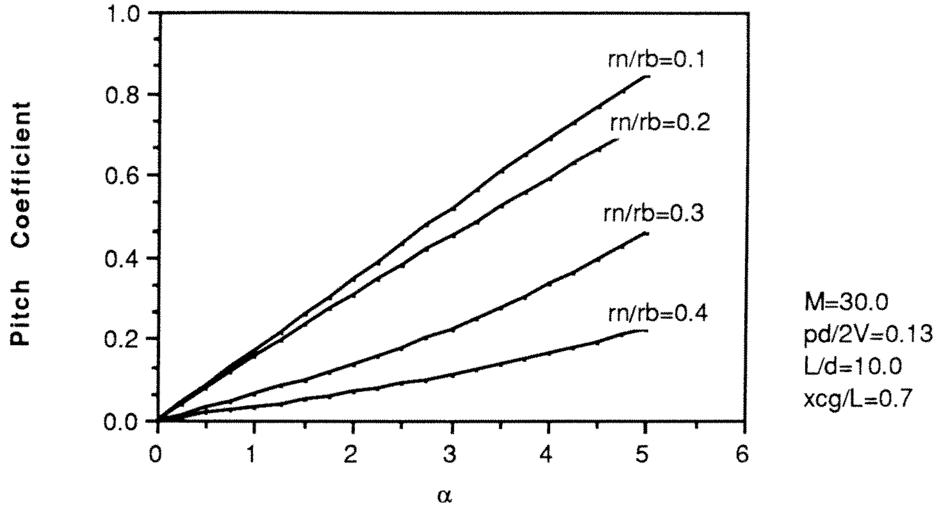

Figure 26. Pitch Coefficient for Varying r_n / r_b

Fig. 27 shows the normal and pitch derivatives that verify this conclusion. The damping derivative is shown in Fig. 28, where it can be seen that nose blunting is dynamically destabilizing.

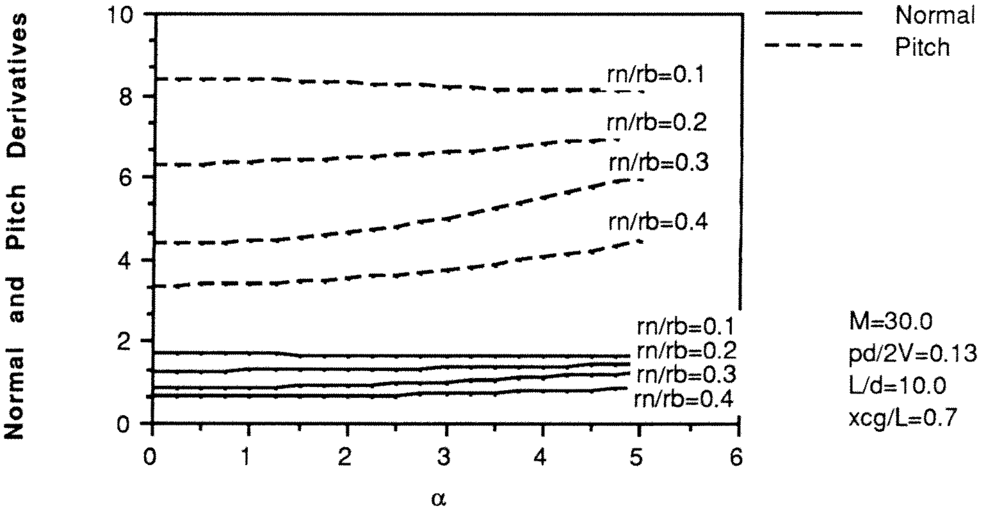

Figure 27. Normal and Pitch Derivatives for Varying r_n / r_b

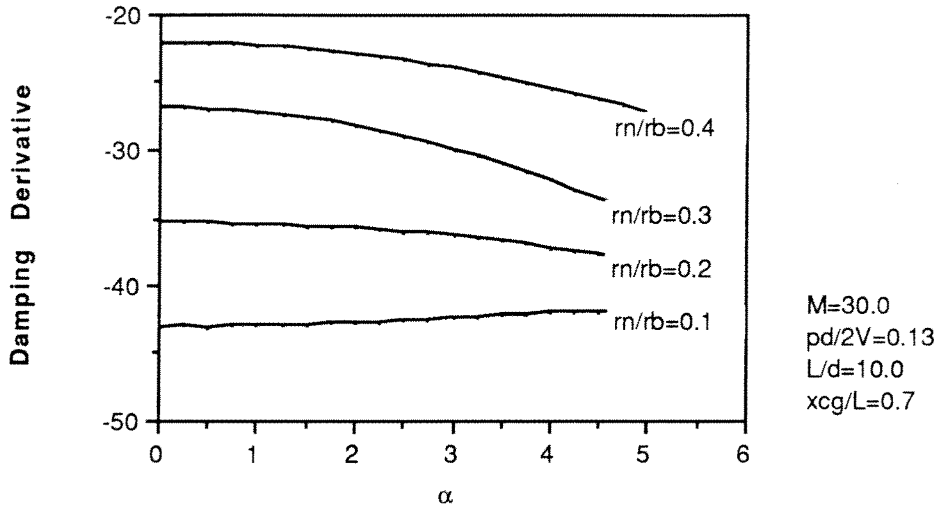

Figure 28. Damping Derivative for Varying r_n / r_b

Fig. 29 shows the Magnus force and moment coefficients. The Magnus force is not too sensitive to the effects of nose blunting, however the moment created is larger for the blunted bodies due to the thicker boundary layer over the forebody.

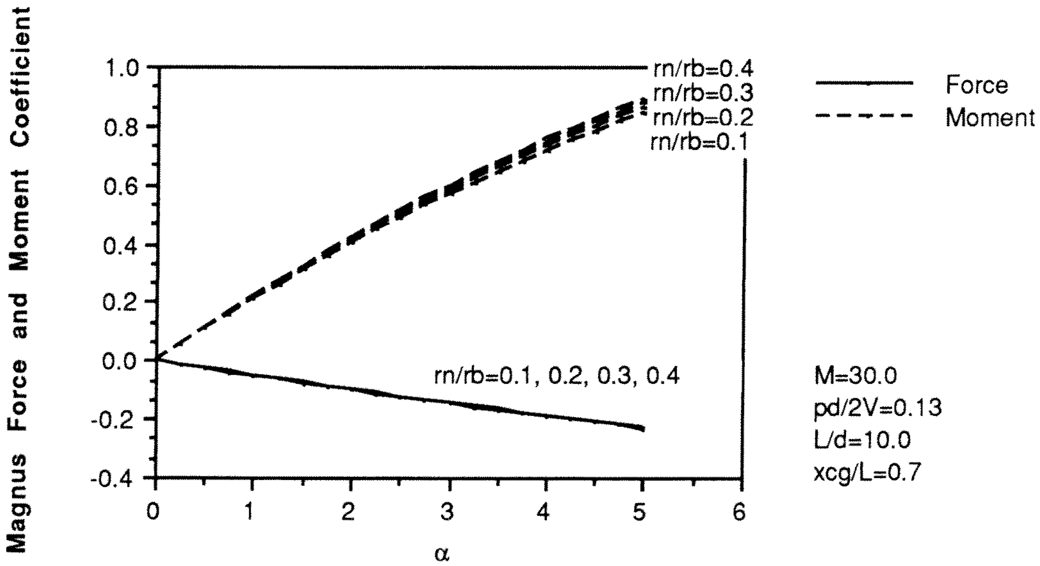

Figure 29. Magnus Force and Moment Coefficients for Varying r_n / r_b

7.2.3 Overall Vehicle Length Variation

The overall vehicle length is also an important parameter in determining vehicle force coefficients, and its effects are even more pronounced for the stability derivative coefficients. Fig. 30 shows the small variation of the axial and normal force coefficients C_A and C_N, and Fig. 31 shows the variation of the pitch coefficient C_m. It should be noted that although the vehicle L/d was changed, the center of gravity $x_{cg}/d = 0.7$ condition was maintained. As might be expected the pitch coefficient for a long vehicle is substantially higher than for a short vehicle, and as shown in Fig. 32, the pitch derivative C_{m_α} for an L/d = 9.0 vehicle is almost twice that for an L/d = 6.0 vehicle. Hence a longer vehicle is much more statically unstable and requires a higher rate of spin for stability. The damping derivative C_{m_θ} is shown in Fig. 33, and it is shown that a short vehicle is much less damped than a longer vehicle.

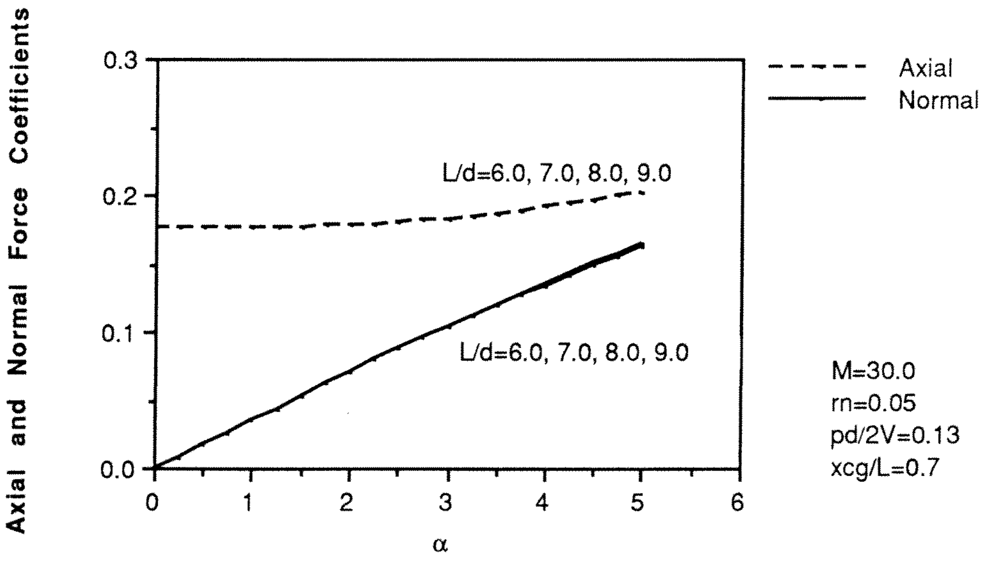

Figure 30. Axial and Normal Force Coefficient for Varying L/d

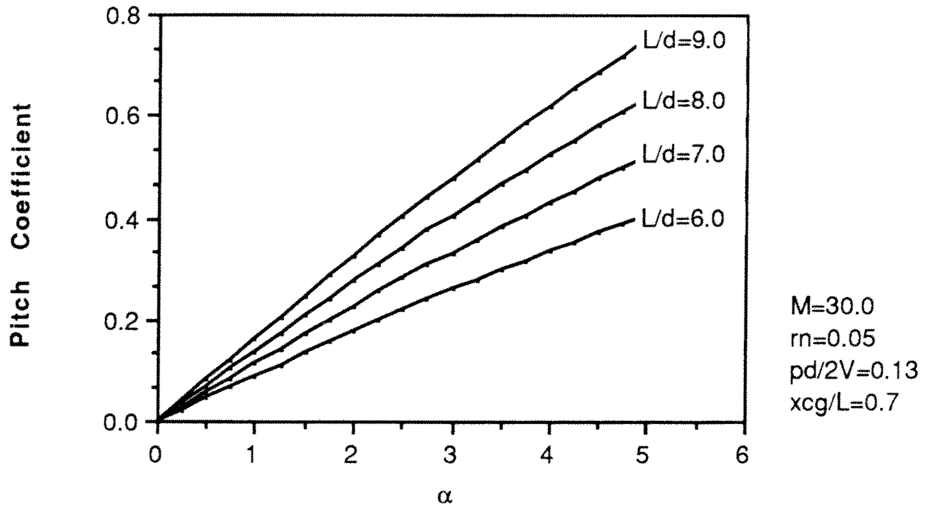

Figure 31. Pitch Coefficient for Varying L/d

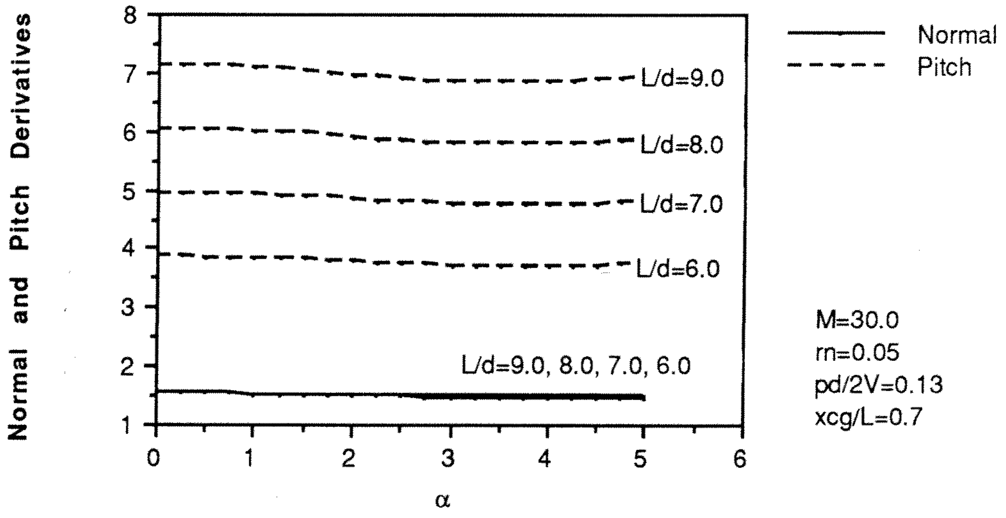

Figure 32. Normal and Pitch Derivatives for Varying L/d

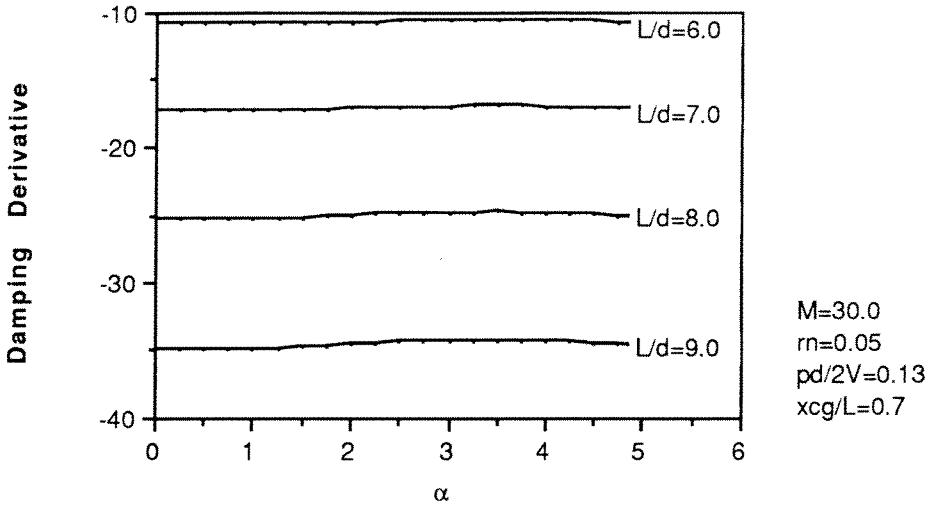

Figure 33. Damping Derivatives for Varying L/d

The significant effects of vehicle length on the Magnus force and moment coefficients are shown in Fig. 34. An L/d = 9.0 vehicle has more than three times the Magnus force and more than ten times the Magnus moment of an L/d = 6.0 vehicle. This is because the magnitude of the Magnus force is directly proportional to the thickness of the boundary layer , and the boundary layer over a short vehicle is thinnner than for a long vehicle. In addition, the force acts over a reduced vehicle surface area which gives a smaller moment as well. The contribution of the afterbody to the Magnus terms is much greater than that of the conical forebody, and hence a short vehicle will contribute less to the Magnus term. For vehicles with the same length forebody and afterbody the contributions of the conical section are only 30%. Since the Magnus moment is such an important effect in terms of vehicle stability, a short vehicle will be much more dynamically stable than a long vehicle. Hence shortening the vehicle greatly affects the static and dynamic stability.

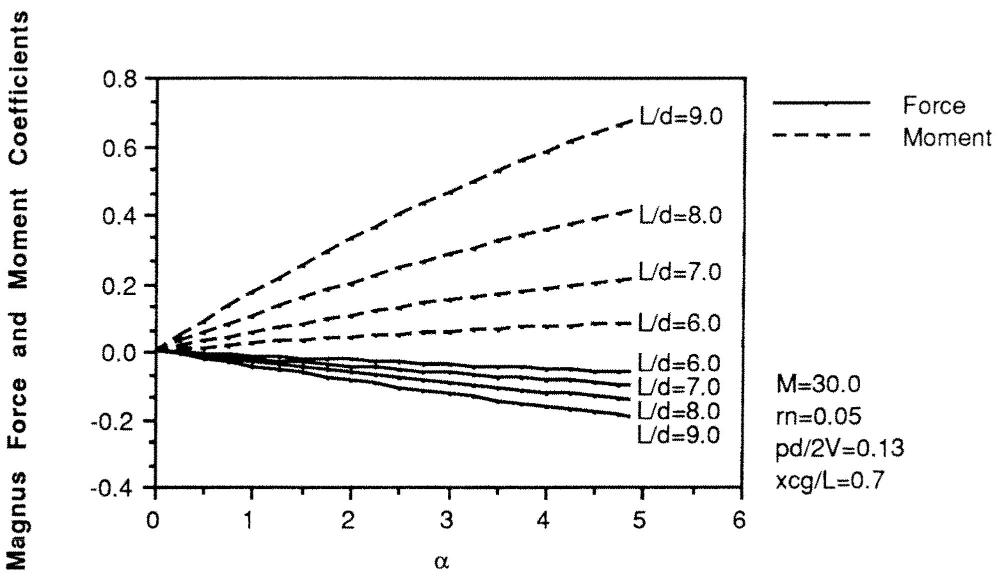

Figure 34. Magnus Force and Moment Coefficients for Varying L/d

7.2.4 Position of Center of Gravity

The effect of changing the position of the center of gravity is shown in Figures 35-38. The value of the aerodynamic forces are not changed, since they are functions only of the exterior configuration, but the moments are changed dramatically. The position of the center of gravity is therefore one of the most critical parameters for determining vehicle stability. The overall vehicle length is maintained at L/d=10.0. Figure 35 shows the significant variation in the pitch coefficient C_m that accompanies x_{cg}/d changes. As the center of mass is moved forward, the pitch coefficient, C_m, and the pitch derivative, C_{m_α}, shown in Fig. 36, are reduced dramatically. This is as is expected, since moving the center of mass nearer to the center of pressure tends to reduce the moment. It is interesting to note that even at $x_{cg}/L = 0.2$ the pitch derivative is positive, and hence the vehicle is statically unstable. This implies that the vehicle center of pressure is even further forward than this point. When the pitch moment coefficient C_m is divided by the normal force coefficient C_N we find that the center of pressure for this configuration at 1^o angle of attack is approximately at $x_{cg}/L = 0.18$. This seems suspect at first, but if we re-examine Fig. 8 we see that the pressure coefficient is largest for $x_{cg}/L \leq 0.25$. Further, there is a large pressure coefficient in the immediate vicinity of the stagnation region. This acts to move the center of pressure even further forward.

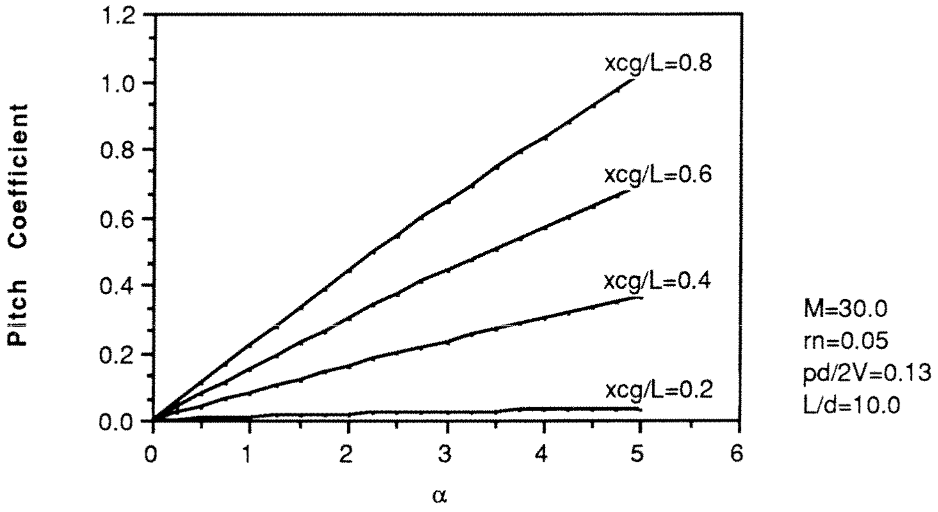

Figure 35. Pitch Coefficient for Varying x_{cg} / L

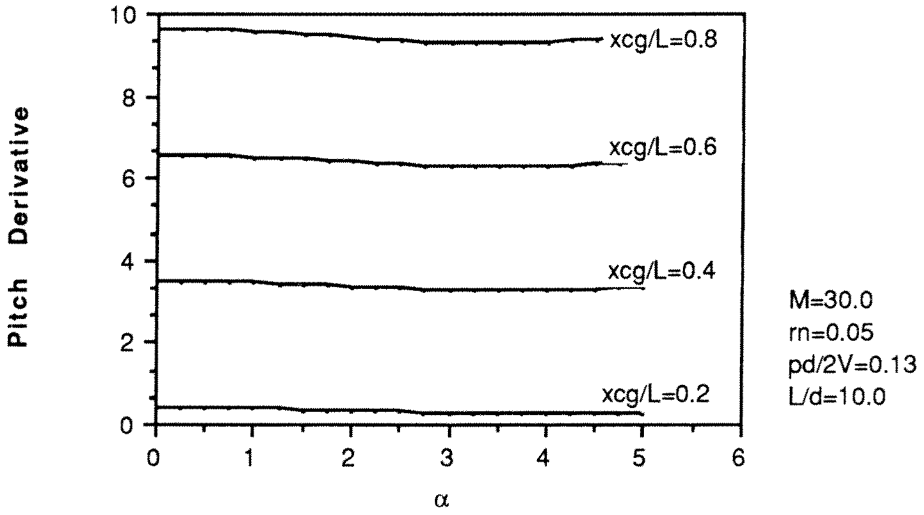

Figure 36. Pitch Derivative Coefficient for Varying x_{cg}/L

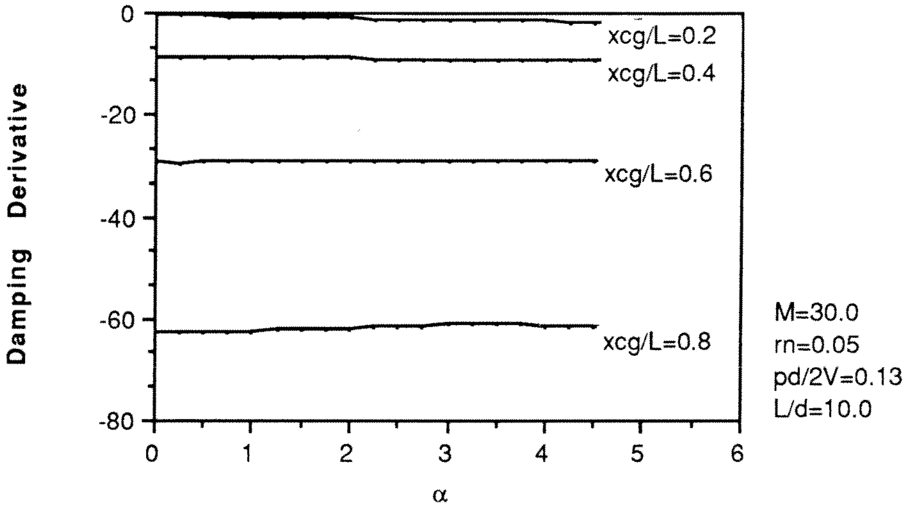

Figure 37. Damping Derivative for Varying x_{cg}/L

The damping derivative C_{m_θ} is shown in Fig. 37, and it can be seen that it is the highest for cases where the center of gravity is further back. Figure 38 shows the Magnus force and moment coefficients C_{Y_p} and C_{N_p}. These decrease with increasing x_{cg}/L. Hence the movement of the center of gravity back is seen to be a dynamically stabilizing effect in terms of the Magnus effects. There are thus two competing effects. Moving the center of gravity forward increases the static stability, and moving the center of gravity back increases the dynamic stability due to Magnus effects. In fact, vehicles that are statically unstable have been made dynamically stable by moving the center of gravity back to counter the strong Magnus effects [2].

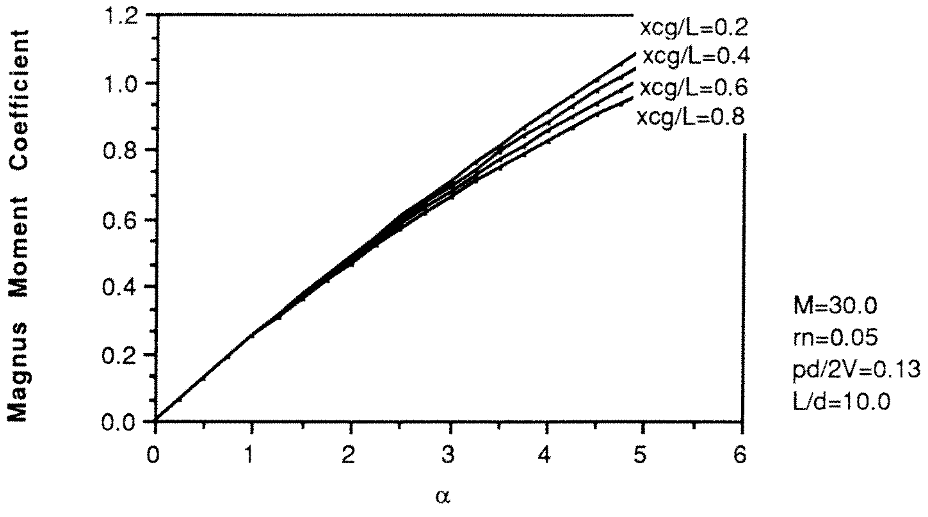

Figure 38. Magnus Moment Coefficient for Varying x_{cg}/L

7.2.5 Miscellaneous Effects

This section will discuss the various miscellaneous effects that have to be accounted for in a complete theory, that have not been included here. They include flow structure such as separation, nonlinearity of the aerodynamic coefficients in pitch and yaw, Reynolds number effects, and atmospheric density gradients for an ascending vehicle.

One of the implicit assumptions in the preceding analysis has been that the flow remains attached to the body. This condition can be satisfied at the lower angles of attack, however at the higher angles flow separation effects cannot be neglected. The effects on stability derivatives are such that separation is statically and dynamically destabilizing. In addition, it may be that flow separation will act to reduce the Magnus force, since the boundary layer separation will act to reduce the pressure gradients. The effects of separation are not, however, predicted by the theory of Vaugn and Reiss [31].

The effects of pitch and yaw are assumed to be linear, i.e. the contributions of pitch and yaw to vehicle stability are assumed to act independently. Since most of the non-linear mechanics investigations have centered on two degree of freedom systems [43] they are not applicable to the sixth order system being considered here. For atmospheric transit of a gyroscopically stable vehicle the effect of a mildly nonlinear moment is to change the frequency of the motion. For cases with large nonlinear effects the small perturbation analysis of Ref. 43 is invalid, and no prediction can be made on vehicle dynamics. Strong nonlinearities also affect the damping characteristics of axisymmetric vehicles, and are essentially independent of the initial conditions.

The effects of Reynolds number change on the vehicle at this high Mach number are not significant. The Reynolds number is on the order of 10^9 and the flow is highly turbulent. The transition point is in the immediate vicinity of the blunted tip, and the flow is certainly turbulent at any point past the sonic line. The flow for any change in Reynolds number would still be in the turbulent flow regime, and the effects of viscous interactions caused by transitions do not need to be considered. The aerodynamic force coefficients most likely to be affected by Reynolds number changes are the Magnus terms, where the magnitude of the forces is directly proportional to the boundary layer thickness. There is also a slight increase in dynamic stability associated with decreasing Reynolds number. As Re decreases, the pitch damping coefficient will increase, providing for a more stable vehicle.

When the vehicle is ascending in a negative density gradient the damping characteristics of the configuration are changed. For an ascending gyroscopically unstable vehicle the effect is to damp the motion , hence the effects of a negative density gradient is stabilizing to an unstable vehicle. The converse is true for a statically stable vehicle, and the effects of decreasing density are to destabilize the vehicle by reducing the damping.

It should be noted that the vehicle design considered here did not include a boatail since the Embedded Newtonian theory cannot account for negative body angles. The effects of a boatail in hypersonic flow have been considered by Daniel and Milton [42]. In terms of stability considerations, for a fixed length vehicle the effects of boatailing are destabilizing. The effects of a boatail are to move the center of pressure forward, creating a larger pitch moment. In addition, a vehicle with a boatail will have a different mass center and moment of inertia which will tend to destabilize the vehicle. The importance of these effects is discussed in Section 7.3.

7.2.6 Heat Transfer

The heat transfer analysis of Chapter 5 was presented in light of its contribution to vehicle stability in terms of nose bluntness effects. In the analysis of Chapter 5 it was assumed that the effects of radiation and convection could be treated separately, however this is not the case.

In a situation where the ablation rate is high, the layer of ablative gases formed at the surface of the vehicle will act to block the effects of convection. This is because the blowing layer thickness is much greater than the viscous layer thickness and the flow cannot reach the surface, as shown in Fig. 7. The only transport mechanism for heating will therefore be radiation.

If, however, we consider the Goulard number, a ratio of the radiant energy to the energy of the flow:

$$\Gamma = \frac{2\,\sigma\,T^4}{\frac{1}{2}\,\rho\,U^3} \qquad 7.2.6.1$$

we find that at sea level, where the radiant energy is expected to be the highest, it has a value of $\Gamma = 7.5 \times 10^{-3}$. This implies that the convective heating effects would be much more dominant than the radiative effects at the stagnation region, as is borne out in the previous results.

Because the mass flow rate of the ablative products is low, we cannot rule out convection as a heat transfer mechanism, since the blowing layer may not be effective in blocking the convective contribution. At the same time, the effects of radiation are not negligible and must also be included. Hence, the complete model must include both radiative and convective heat transfer effects.

7.3 A Stable Configuration

Based on the preceding stability considerations an attempt was made to select a vehicle that would be statically and dynamically stable. Such a configuration could not be found at the present time. The most stable configuration found consists of an overall body length of L/d = 6.5, a center of mass position $x_{cg}/L = 0.6$, and a bluntness ratio $r_n/r_b = 0.2$. This configuration yields a dynamic stability factor $S_d = 18.4$ and requires a spin rate of 6300 rad/sec for static stability. The drag penalty of the blunter nose radius was not great, and was acceptable based on its effects of improving the static stability.

Altering the configuration of the vehicle allowed the aerodynamic coefficients to be selectively changed, however the defeating element in meeting the stability factor constraints is the change of the mass distribution of the vehicle. The vehicle mass was kept constant during the configuration changes, and a homogeneous mass distribution was assumed. This produced moments of inertia for the vehicle that could not satisfy the dynamic stability factor of Equation 6.2.1 with any combination of aerodynamic coefficients. All configurations could satisfy the gyroscopic stability factor with sufficient spin.

Based on the parametric study of vehicle configurations it was found that a vehicle's dynamic stability could be improved by reducing the overall length of the vehicle and by selective positioning of the center of mass. The effects of changing the center of mass, however, are not straight forward. Selecting a center of mass to minimize the pitching moment and to maximize the pitch damping does not necessarily result in a stable configuration, as the important effects of changing the moments of inertia must be considered also. Based on the form of the dynamic stability factor, we would like a larger moment of inertia I_x and a smaller moment of inertia I_y than can be given by the current mass distribution. Since this analysis considered only the case of a homogeneous mass distribution the results must be qualified to indicate that a stable configuration cannot be found for this situation only. In an actual Ram Accelerator Mass Launcher vehicle the mass distribution might be such that a configuration may be found that could be stable, however this cannot be determined at present.

Chapter 8

Conclusions and Recommendations

It has been shown through the numerical integration of the equations of motion that the current Ram Accelerator Mass Launcher vehicle is dynamically unstable, and that it cannot be spin stabilized with any vehicle rotation. The mass loss due to ablation for a launch velocity of 10,000 m/sec at sea level, and a flightpath angle of 20°, was found to be only 2.0 kg. It was shown that the effects of radiative and convective heating must both be considered. The effects of ablation on vehicle stability are found to not be important, and the small increase in nose blunting that occurs is stabilizing.

Based on the preceding analysis it is recommended that any Ram Accelerator Mass Launcher vehicle be actively stabilized. This would have the added advantage of simplifying the aerodynamic force system since vehicle spin would no longer be required, and the Magnus terms would not contribute to instability. Many types of active control systems exist which could perform this function, ranging from simple fins to reaction jets.

Although a contribution to determining the stability of the Ram Accelerator Mass Launcher was made, it is necessary for future efforts to include an investigation of vehicles with nonhomogeneous mass distributions in order to investigate a more realistic situation. Considerations for these investigations must also include a more detailed investigation of flow separation effects and boatailing.

REFERENCES

1. Fowler, R. H., Gallop, E. G., Lock, C. N. H, and Richmond, H. W., "The Aerodynamics of a Spinning Shell," Philosophical Transactions of the Royal Society of London, 1920.

2. McShane, E. J., Kelley, J. L., and Reno, F. V., Exterior Ballistics, The University of Denver Press, 1953.

3. Davis, L., Follin, J. W., and Blitzer, L., Exterior Ballistics of Rockets, D. Van Nostrand Company, Inc., 1958.

4. Kaloupis, P., and Bruckner, A. P., "The Ram Accelerator: A Chemically Driven Mass Launcher," AIAA Paper No. 88-2968, July 1988.

5. Bruckner, A. P., and Hertzberg, A., "Ram Accelerator Direct Launch System for Space Cargo," IAF Paper No. 87-211, September 1987.

6. Bruckner, A. P., and Hertzberg, A., eds., "Design of a Ram Accelerator Mass Launch System," Final Report, NASA/USRA Advanced Space Design Program, University of Washington, Seattle, WA, 1988.

7. Hertzberg, A., Bruckner, A. P., and Bogdanoff, D. W., "Ram Accelerator: A New Chemical Method for Accelerating Projectiles to Ultrahigh Velocities," AIAA Journal, Vol. 26, pp. 195-203, February 1988.

8. Bruckner, A. P., Bogdanoff, D. W., Knowlen, C., and Hertzberg, A., "Investigation of Gasdynamic Phenomena Associated with the Ram Accelerator Concept," AIAA Paper No. 87-1327, June 1987.

9. Knowlen, C., Bruckner, A. P., Bogdanoff, D. W., and Hertzberg, A., "Performance Capabilities of the Ram Accelerator," AIAA Paper No. 87-2152, July 1987.

10. Hertzberg, A., Bruckner, A. P., Bogdanoff, D. W., and Knowlen, C., "The Ram Accelerator and its Applications: A New Chemical Approach for Reaching Ultrahigh Velocities," Proceedings of the 16th International Symposium on Shock Tubes and Waves, Aachen, West Germany, July 1987.

11. Bruckner, A. P., Knowlen, C., Scott, K. A., and Hertzberg, A., "High Velocity Modes of the Thermally Choked Ram Accelerator Concept, AIAA Paper 88-2925, July 1988.

12. Burnham, E. A., "Experimental and Numerical Analysis of the Thermally Choked Ram Accelerator Starting Process," Master of Science Thesis, University of Washington, Seattle, WA, 1989.

13. Etkin, B., Dynamics of Atmospheric Flight, John Wiley & Sons, Inc., 1972.

14. Liepmann, H. W., and Roshko, A., Elements of Gas Dynamics, GALCIT Aeronautical Series, John Wiley & Sons, Inc., pp. 206-224, 1957.

15. Van Dyke, M. D., "First and Second Order Theory of Supersonic Flow Past Bodies of Revolution," Journal of the Aeronautical Sciences, pp. 161-216, March 1951.

16. Hayes, W. D., and Probstein, R. F., Hypersonic Flow Theory I, Inviscid Flows, Academic Press, pp. 201-206, 1966.

17. Busemann, A., Handworterbuck der Naturwissenschaften IV, Flussigkeits und Gasbewegung, Gustav Fisher, pp. 244-279, 1933.

18. Seiff, A., "Secondary Flow Fields Embedded in Hypersonic Shock Layers," NASA TN D-1304, 1962.

19. Ericsson, L. E., and Scholnick, I. M., "Effect of Nose-Bluntness on the Hypersonic Unsteady Aerodynamics of Flared and Conical Bodies of Revolution," Journal of Spacecraft and Rockets, Vol. 6, pp. 321-324, March 1969.

20. Ericsson, L. E., "Unsteady Embedded Newtonian Flow," Acta Astronautica, Vol. 18, No. 5, pp. 309-330, 1973.

21. Ericsson, L. E., "Generalized Unsteady Embedded Newtonian Flow," Journal of Spacecraft and Rockets, Vol. 12, pp. 718-726, December 1975.

22. Ericsson, L. E., "Hyperballistic Vehicle Design," Journal of Spacecraft and Rockets, Vol. 19, pp. 496-505, Nov. - Dec. 1982.

23. Tong, B. G., and Hui, W. H., "Unsteady Embedded Newton-Busemann Theory," Journal of Spacecraft and Rockets, Vol. 23, pp. 129-135, March - April 1986.

24. East, R. A., and Hutt, G. R., "Comparison of Predictions and Experimantal Data for Hypersonic Pitching Motion Stability," Journal of Spacecraft and Rockets, Vol. 25, pp. 225-233, May - June 1982.

25. Sedney, R., "Laminar Boundary Layers on a Spinning Cone at Small Angles of Attack in a Supersonic Flow," Journal of the Aeronautical Sciences, Vol. 24, pp. 430-436, June 1957.

26. Clark, B. L., "Navier-Stokes Solutions for Laminar Incompressible Flow Over Yawed Spinning Bodies of Revolution," AIAA Paper No. 72-112, January 1972.

27. Dwyer, H. A., and Sanders, B. R., "Magnus Forces on Spinning Supersonic Cones-Part : The Boundary Layer," AIAA Journal, Vol. 14, No. 4, pp.498-504, 1976.

28. Agarwal, R. K., "Computation of Supersonic Turbulent Flow Past a Spinning Cone," AIAA Paper No. 82-0304, January 1982.

29. Kegelman, J. T., Nelson, R. C., and Mueller, T. J., "Boundary Layer and Side Force Characteristics of a Spinning Axisymmetric Body," AIAA Paper No. 80-1584, January 1980.

30. Sturek, W. B., Mylin, D. C., and Bush, C. C., "Computational Parametric Study of the Aerodynamics of Spinning Slender Bodies at Supersonic Speeds," Technical Report No. ARBRL-TR-02358, U.S. Army Armament Research and Development Command, Ballistic Research Laboratory, Aberdeen Proving Ground, Maryland, August 1981.

31. Vaugn, H. R., Reis, G. E., "A Magnus Theory," AIAA Journal, Vol. 11, No. 10, pp. 1396-1403, October 1973.

32. Milton, J. E., "Aerodynamic Characteristics of Hypersonic Spin Stabilized Projectiles," AIAA Paper No. 82-0052, January 1982.

33. Ragsdale, W. C., and Horanoff, E. V., "Investigation of a Side Force Due to Ablation," AIAA Journal, Vol. 13, No. 9, September 1976.

34. Waterfall, A. P., "Effect of Ablation on the Dynamics of Spinning Re-Entry Vehicles," Journal of Spacecraft and Rockets, Vol. 6, No. 9, pp. 1038-1047, 1969.

35. Roshenow, W. M., Hartnett, J. P., Ganic, E. N., Handbook of Heat Transfer Fundamentals, McGraw Hill Book Company, 1985.

36. Park, C., and Bowen, S. W., "Ablation and Deceleration of Mass Driver Projectiles for Space Disposal of Nuclear Wastes," AIAA Paper No. 81-0355, January 1981.

37. Wilkins, M. E., and Tauber, M. E., "Boundary Layer Transitions on Cones at Speeds up to 7 km/sec," AIAA Journal, Vol. 4, No. 8, pp. 1344-1348, August 1966.

38. Tauber, M. E., "A Review of High Speed Convective Heat Transfer Computation Methods," NASA TN 2914, July 1989.

39. Putz, K. E., and Bartlett, E. P., "Heat Transfer and Ablation Rate Correlations for Re-Entry Heat Shield and Nose-Tip Applications," Journal of Spacecraft and Rockets, Vol. 10, No. 1, pp. 15-22, January 1973.

40. Probstein, R. F., "Radiation Slip," AIAA Journal, Vol. 1, No. 5, pp. 1202-1204, May 1963.

41. Moeckel, W. E., and Weston, K. C., "Composition and Thermodynamic Properties of Air in Chemical Equilibrium," NACA TN 4265, April 1958.

42. Daniel, D. C., and Milton, J. E., "A Drag and Stability Analysis of Hypersoni Spin Stabilized Projectiles," AIAA Paper No. 80-1587, January 1980.

43. Murphy, C. H., "The Prediction of Non-Linear Pitching and Yawing Motion of Symmetric Missiles," Journal of the Aeronautical Sciences, Vol. 24, No. 7, pp. 473-479, July 1957.

APPENDIX A:
EQUATIONS OF MOTION

The simultaneous eqautions of motion that need to be solved for determining vehicle motion are presented here. Prior knowledge of the forces and moments is assumed, and the initial conditions are:

$$\begin{gathered}(\lambda, \mu, R)\\(u, v, w)\\(\theta, \phi, \psi)\\(p, q, r)\end{gathered} \tag{A.1}$$

These specify the position, attitude, and velocity of the vehicle in body axes. R represents the geocentric altitude. The equations are as follows:

$$\begin{bmatrix} p_B^E \\ q_B^E \\ r_B^E \end{bmatrix} = \mathbf{L}_{BV} \begin{bmatrix} \cos\lambda \\ 0 \\ -\sin\lambda \end{bmatrix} \omega^E \tag{A.2}$$

$$\begin{bmatrix} X \\ Y \\ Z \end{bmatrix} = -\mathbf{L}_{BV} \begin{bmatrix} D \\ C \\ L \end{bmatrix} \tag{A.3}$$

Here the forces D, C, and L are the drag, side, and lift forces in the vehicle axes system. The force equations can be writen:

$$X - m\,g\,\sin\theta = m\,[\,\dot{u} + (q_B^E + q)\,w - (r_B^E + r)\,v\,] \tag{A.4a}$$

$$Y + m\,g\,\cos\theta\,\sin\phi = m\,[\,\dot{v} + (r_B^E + r)\,u - (p_B^E + p)\,w] \tag{A.4b}$$

$$Z + m\,g\,\cos\theta\,\cos\phi = m\,[\,\dot{w} + (p_B^E + p)\,v - (q_B^E + q)\,u\,] \tag{A.4c}$$

$$L = I_x\,\dot{p} \tag{A.5a}$$

$$M = I_y\,\dot{q} - (I_z - I_x)\,r\,p \tag{A.5b}$$

$$N = I_z\,\dot{r} - (I_x - I_y)\,p\,q \tag{A.5c}$$

$$\begin{bmatrix} \dot{\lambda}\, R \\ \dot{\mu}\, R \cos\lambda \\ -\dot{R} \end{bmatrix} = \mathbf{L}_{VB} \begin{bmatrix} u \\ v \\ w \end{bmatrix} \qquad \text{A.6}$$

$$\begin{bmatrix} P \\ Q \\ R \end{bmatrix} = \begin{bmatrix} p \\ q \\ r \end{bmatrix} - \mathbf{L}_{BV} \begin{bmatrix} \left(\omega^{E} + \dot{\mu}\right) \cos\lambda \\ -\dot{\lambda} \\ -\left(\omega^{E} + \dot{\mu}\right) \sin\lambda \end{bmatrix} \qquad \text{A.7}$$

$$\begin{bmatrix} \dot{\phi} \\ \dot{\theta} \\ \dot{\psi} \end{bmatrix} = \begin{bmatrix} 1 & \sin\phi \tan\theta & \cos\phi \tan\theta \\ 0 & \cos\phi & -\sin\phi \\ 0 & \sin\phi \sec\theta & \cos\phi \sec\theta \end{bmatrix} \begin{bmatrix} P \\ Q \\ R \end{bmatrix} \qquad \text{A.8}$$

$$u = u_o + \int_{t1}^{t2} \dot{u}\, dt \quad , \quad v = v_o + \int_{t1}^{t2} \dot{v}\, dt \quad , \quad w = w_o + \int_{t1}^{t2} \dot{w}\, dt \qquad \text{A.9}$$

$$p = p_o + \int_{t1}^{t2} \dot{p}\, dt \quad , \quad q = q_o + \int_{t1}^{t2} \dot{q}\, dt \quad , \quad r = r_o + \int_{t1}^{t2} \dot{r}\, dt \qquad \text{A.10}$$

$$\lambda = \lambda_o + \int_{t1}^{t2} \dot{\lambda}\, dt \quad , \quad \mu = \mu_o + \int_{t1}^{t2} \dot{\mu}\, dt \quad , \quad R = R_o + \int_{t1}^{t2} \dot{R}\, dt \qquad \text{A.11}$$

$$\theta = \theta_o + \int_{t1}^{t2} \dot{\theta}\, dt \quad , \quad \phi = \phi_o + \int_{t1}^{t2} \dot{\phi}\, dt \quad , \quad \psi = \psi_o + \int_{t1}^{t2} \dot{\psi}\, dt \qquad \text{A.12}$$

$$\rho = \rho_o\, e^{-\beta z} \qquad \text{A.13}$$

The transformation matrix $\mathbf{L}_{BV}$ between coordinate systems can be given by:

$$\mathbf{L}_{BV} = \begin{bmatrix} \cos\theta\cos\psi & \cos\theta\sin\psi & -\sin\theta \\ \sin\phi\sin\theta\cos\psi - \cos\phi\sin\psi & \sin\phi\sin\theta\sin\psi + \cos\phi\cos\psi & \sin\phi\cos\theta \\ \cos\phi\sin\theta\cos\psi + \sin\phi\sin\psi & \cos\phi\sin\theta\sin\psi - \sin\phi\cos\psi & \cos\phi\cos\theta \end{bmatrix} \qquad \text{A.14}$$

where the inverse matrix $\mathbf{L}_{VB} = \mathbf{L}_{BV}^{-1} = \mathbf{L}_{BV}^{T}$ since they are orthogonal matrices.

APPENDIX B: UNSTEADY AERODYNAMIC DERIVATIVES

The functions that are used to find the nonsteady contributions of variations in angle of attack for the embedded pressure coefficients can be given by [22]:

$$(C_{p_{\alpha}})_1 = C_\gamma \frac{\partial C_{p_{newt}}}{\partial \alpha} f^* \qquad \text{B.1a}$$

$$(C_{p_{\alpha}})_2 = \frac{\partial C_{p_o}}{\partial C_{DN}} \frac{\partial C_{DN}}{\partial \alpha} \qquad \text{B.1b}$$

$$\left(\Delta^i C_{p_\alpha}\right)_1 = C_\gamma \, C_{p_{newt}} \frac{\partial f^*}{\partial\left(\frac{\Delta z}{d_n}\right)} \frac{\partial\left(\frac{\Delta z}{d_n}\right)}{\partial \alpha} \qquad \text{B.1c}$$

$$\left(\Delta^i C_{p_\alpha}\right)_2 = C_\gamma \, C_{p_{newt}} \frac{\partial f^*}{\partial C_{DN}} \frac{\partial C_{DN}}{\partial \alpha} \qquad \text{B.1d}$$

$$(C_{p_q})_1 = \frac{\partial C_{p_E}}{\partial\left(\frac{v}{u}\right)} \frac{\partial\left(\frac{v}{u}\right)}{\partial\left(\frac{d\,q}{U_\infty}\right)} \qquad \text{B.2a}$$

$$(C_{p_q})_2 = \frac{\partial C_{p_o}}{\partial C_{DN}} \frac{\partial C_{DN}}{\partial\left(\frac{v}{u}\right)} \frac{\partial\left(\frac{v}{u}\right)}{\partial\left(\frac{d\,q}{U_\infty}\right)} \qquad \text{B.2b}$$

$$\left(\Delta^i C_{p_{\dot\alpha}}\right)_1 = - \frac{x_{CG}}{d\,g^*} \left(\Delta^i C_{p_\alpha}\right)_1 \qquad \text{B.2c}$$

$$\left(\Delta^i C_{p_{\dot\alpha}}\right)_2 = - \frac{x_{CG}}{d\,g^*} \left(\Delta^i C_{p_\alpha}\right)_2 \qquad \text{B.2d}$$

where for a spherical nosetip

$$\frac{\partial C_{DN}}{\partial \alpha} = 0 \qquad \text{B.3}$$

and the dynamic derivative of (v / u) is just:

$$\frac{\partial\left(\frac{v}{u}\right)}{\partial\left(\frac{d\,q}{U_\infty}\right)} = \frac{d_n}{d}\left(\frac{C_{m_\alpha}}{C_{N_\alpha}}\right)_n \qquad \text{B.4}$$